Review

DFT flavor of coordination chemistry

Athanassios C. Tsipis *

Laboratory of Inorganic and General Chemistry, Department of Chemistry, University of Ioannina, 451 10 Ioannina, Greece

Contents

ARTICLE INFO

ABSTRACT

An overview of recent progress in DFT application to coordination chemistry is presented. Some recent applications that best illustrate the promise of DFT in a number of very active areas of coordination chemistry, such as catalysis (mechanistic studies), bonding (electronic and bonding character) electronic spectroscopy (absorption and emission spectra) and heavy-nucleus NMR spectroscopy are reviewed. Particular emphasis was given to the practical aspects that may be interesting for experimentalists that wish to employ DFT alongside to their experimental work. General instructions of how to select the proper DFT computational protocol for a particular study are outlined.

© 2014 Elsevier B.V. All rights reserved.

* Tel.: +30 2651008333.
  E-mail address: attsipis@uoi.gr

Nomenclature

ACFD	adiabatic connection fluctuation-dissipation theorem
AE	adiabatic energies
AHS	atomic Hirshfeld surface
AIM	atoms in molecules
aiMD	ab initio molecular dynamics
B2PLYP	double hybrid functional
B3LYP	Becke's three-parameter exchange with Lee, Yang, and Parr correlation functional
BLYP	Becke's 1988 exchange functional with the correlation functional of Lee, Yang, and Parr
BP86	Becke–Perdew GGA
B97-D3	dispersion-corrected B97 functional
B97XD	range-separated functional
ω-B97XD	range-separated functional
BLYP-D3	dispersion-corrected BLYP functional
BCP	bond critical point
BS	broken Symmetry
CAM-B3LYP	Coulomb-attenuating method-B3LYP
CASPT2	complete active space second-order perturbation theory
CASSCF	complete active space self-consistent field
CBS	complete basis set
ccCA-TM	correlation consistent Composite Approach for transition metals
CC	coupled cluster
CCP	cage critical point
CCSD	coupled cluster with singles and doubles
CCSD(T)	CC with single and double excitations augmented with perturbatively calculated triples
CDA	charge decomposition analysis
CEP-31G(5d,7f)	Stevens/Basch/Krauss ECP split valance basis set
CMD	concerted metalation-deprotonation pathway
COSMO	conductor-like screening model
COSMO-RS	COSMO for realistic solvation
C-PCM	conductor-like PCM solvation model
CPs	critical points
CR	completely renormalized
CS	chemical Shift tensor
CTCs	cyclic trinuclear complexes
DE	diabatic energies
def2-SVP	basis set of the def2-type
DFs	density functionals
DFT	density functional theory
DFT-D3	dispersion-corrected conventional DFs
DFT-dDXDM	density dependent dispersion corrected conventional DFs
DFT-dDsC	density-dependent energy correction of a conventional functional
DHDFs	double-hybrid density functionals
DKH	Douglas–Kroll–Hess Hamiltonian
D-PCM	dielectric version of PCM
DSD-BLYP	dispersion corrected, spin-component scaled double hybrid-BLYP
ECP	efective-core potential
EDA	energy decomposition analysis
EF	Eigenvalue-following
ELF	electron localization function
ELI-D	electron localizability indicator based on D-restricted partitioning
EOM	equation of motion
EPR	electron paramagnetic resonance
ESID	energy splitting in Dimer model
GC	gas chromatography
GGA	generalized-gradient approximation
GIAO	Gauge-including atomic orbital
GIPAW	Gauge including projection augmented wave
HAHA	heavy-atom effects on heavy atoms
HALA	heavy-atom effects on light atoms
HF	Hartree–Fock approximation
HFCCs	hyperfine coupling constants
HOFs	heat of formations
HOMO	highest occupied molecular orbital
HS	high spin
IEF-PCM	integral-equation-formalism versions of PCM
IM	intermediate
IMOMO	integrated molecular orbital plus molecular orbital method
IPCM	isodensity PCM
IR	infra red
IRC	intrinsic reaction coordinate
IPs	ionization potentials
KS	Kohn–Sham
KS-DFT	Kohn–Sham density functional theory
LACVP	basis sets combining the 6-31G basis set with the LANL2DZ effective core basis set
LANL2DZ	Los Alamos National Laboratory 2-Double-Z
LC-ωPBE	long-range corrected PBE functional
LDA	local density approximation
LED	light emitting diodes
^{3}LLCT	triplet ligand-to-ligand charge transfer
LMCT	ligand-to-metal charge transfer
LMOs	localized molecular orbitals
LR	linear response theory
LR-ESC	linear response elimination of small component
LR-TD-DFT	linear response-time dependent density functional theory
RSCF-CV-DFT	relaxed and self-consistent extension of constricted variational DFT
LSDA	local spin density approximation
LUMO	lowest unoccupied molecular orbital
M05-2X	Minnesota group of functionals
M06-2X	Minnesota group of functionals
MBPT	many-body perturbation theory
MC	metal centered excitations
^{3}MC	Thriplet metal centered excitations
MCSCF	multi-configurational self-consistent-field
MD	molecular dynamics
MEP	molecular electrostatic potential
MLCT	metal-to-ligand charge transfer
^{3}MLCT)	triplet metal-to-ligand charge transfer
MO	molecular orbital
MPA	Mulliken population analysis
MP2	Möller-Plesset perturbation theory of the second order
MS	magnetic shielding tensor
MSBCT	metal-to-sigma-bond-charge-transfer
MS-CASPT2	multi-state complete active space second order perturbation theory
NBO	natural bond orbital analysis
NCP	nuclear critical point
NICS	nucleus-independent chemical shift
NLMOs	natural localized molecular orbitals
NMR	nuclear magnetic resonance

NPA	natural population analysis
NTOs	natural transition orbitals
OEL	organic electro-luminescence
OEP	optimized effective potential
OLED	organic light emitting diodes
OLYP	GGA functional consisting of OptX exchange and LYP correlation functionals
PBE	the Perdew–Burke–Ernzerhof exchange-correlation functional
PCM	polarizable continuum model
PES	potential energy surface
PT2	second order perturbation theory
PW91	Perdew–Wang 91 correlation functional
PW6B95-D3	hybrid PW6B95 functional in combination with D3 diepersion corrections
QZVPP	quadruple-zeta valence double polarization basis set
QM/MM	quantum mechanics/molecular mechanics
OST2, QST3	quadratic synchronous transit methods
QZ4P	relativistically optimized valence quadruple zeta plus four polarization functions
RAS	self-consistent restricted active space
RCP	ring critical point
RDG	reduced density gradient
S	surface area
SBSBCT	sigma-bond-to-sigma-bond-charge-transfer
SCF	self-consistent field
SCI-PCM	self-consistent isodensity PCM model
SCRF	self-consistent reaction field solvation models
SCS-MP2	spin-component-scaled MP2 method
SDD	Stuttgart/Dresden triple zeta ECPs
SD(T)	single, double, and perturbative triple substitutions
SET	single electron transfer
SIE	self-interaction error
SMD	a universal continuum solvation model (D stands for density)
SO	spin–orbit effects
SOC	spin–orbit coupling
SOMO	singly occupied molecular orbital
SS	spin–spin coupling
SSNMR	solid-state nuclear magnetic resonance
TD-DFT	time-dependent density functional theory
TDI	TOF determining intermediate
TDTS	TOF-determining transition state
TOF	turnover frequency
TPSS	meta-GGA functional
TSs	transition states
TZP	triple zeta basis set plus one polarization function
TZ2P	triple zeta basis set plus two polarization functions
TZVP	triple zeta valence polarization basis set
TZVPP	triple zeta valence double polarization basis set
UV–vis	ultraviolet–visible spectra
VEM	vertical excitation model
VWN	the Vosko, Wilk, and Nusair exchange-correlation functional
XAS	X-ray absorption spectroscopy
XES	X-ray emission spectroscopy
ZFS	zero-field-splitting
ZORA	zero order regular approximation

1. Introduction

Over the last few decades density functional theory (DFT) has developed to a stage that can provide invaluable help in the interpretation of experimental measurements of a broad range of molecular properties of coordination compounds. In this context DFT provides a numerical "virtual coordination chemistry lab" able to compute even properties difficult or impossible to measure experimentally. Nowadays, DFT has become a general tool to understand and predict the behavior of a broad range of chemical, physical, and biological phenomena of importance in chemical reactivity, catalytic activity, bioactivity, photophysics, electronic and nuclear-magnetic resonance spectroscopy, linear and nonlinear optics etc. in the realm of coordination chemistry.

Transition metal computational chemistry has been covered quite extensively in special issues of *Chemical Reviews* [1–13] and *Coordination Chemistry Reviews* [14–29]. More recent reviews cover also some specific topics of computational chemistry related to quantum chemical studies of intermediates and reaction pathways in selected metalloenzymes and catalytic synthetic systems [30] and the electronic structures of metal sites in proteins and models [31]. The impact of modern computational technology in the advancement of inorganic chemistry was outlined by Tsipis [32], while a recent *Dalton Transactions* themed issue was devoted to the full breadth of the impact of computational methods on molecular inorganic chemistry, containing a series of papers that highlight applications in small molecule activation, organometallic reactivity, bioinorganic chemistry, the modeling of spectroscopic properties and practical methodological aspects of computational chemistry [33–58]. Timely exhaustive assessment of DFT methods applied in transition metal chemistry has been reviewed by Cramer and Truhlar [59]. Frank Neese [60] provided a detailed account of DFT and its application to the calculation of molecular properties of inorganic compounds. Platas-Iglesias et al. [61] presented an overview of different successful applications of DFT to investigate the structure, dynamics, vibrational spectra, NMR chemical shifts, hyperfine interactions, excited states, and magnetic properties of lanthanide(III) complexes. Maslowsky Jr. [62] reported on the stability, structures and bonding of inorganic "sandwich" compounds or metallocenes in which aromatic, antiaromatic and nonaromatic inorganic rings, as well as those with multiple or conflicting aromaticity, are bonded primarily to the transition elements. A very recent publication in *Coordination Chemistry Reviews* by Kepp [63], offering a discussion of the physical effects and ingredients in functionals, their systematic errors and approaches to deal with them, in order to identify broadly applicable methods for inorganic chemistry is commended to the readers and researchers in the field.

Herein, we present an overview of the most recent successful applications of DFT to investigate the structure, bonding and spectroscopic (absorption and emission spectra, NMR chemical shifts, hyperfine interactions) properties of coordination compounds. Other important theoretical topics relating to the field of coordination chemistry, such as molecular dynamics (MD), including Born-Oppenheimer Molecular Dynamics, enzymatic mechanisms, including Quantum Mechanics/Molecular Mechanics (QM/MM) methods are outside the scope of the present review. As the subject of the applications of DFT to transition metal coordination compounds is too large we selected only recent papers (last decade) that best illustrate the promise of DFT in a number of very active areas of coordination chemistry. Particular emphasis was given to the practical aspects that may be interesting for experimentalists that wish to employ DFT alongside to their experimental work. In this context the present review has also the character of a tutorial review.

2. DFT at work in the coordination chemistry lab

At this point, it is not the intention to describe the theoretical background of the DFT methodology, but rather to familiarize the newcomer to the field of computational coordination chemistry with the practical issues faced under DFT at work.

2.1. Capabilities of DFT

Applying DFT methods, the following operations may be performed:

- Geometry optimization
- Single-point energy calculation
- Predicting barriers and reaction paths (reaction mechanisms)
- Calculation of wave functions and detailed descriptions of molecular orbitals (bonding properties)
- Calculation of atomic charges, dipole moments, multipole moments, electrostatic potentials, polarizabilities, etc.
- Calculation of spin state energetics
- Calculation of magnetic exchange coupling constants of molecular magnets
- Calculation of vibrational frequencies, IR and Raman intensities
- Calculation of NMR chemical shifts
- Calculation of ionization energies and electron affinities
- Time-dependent calculations (optical spectroscopy)
- Simulating EPR spectra
- Simulating X-ray absorption spectra
- Inclusion of the electrostatic effects on solvation.
- Noncovalent interactions in extended molecular systems

2.2. DFT at a glance (basics of the theory)

Since most theoretical studies of coordination and organometallic compounds employ DFT methods we should first define the meaning of the word functional and the theorems on which DFT is truly based to supply the newcomer to the field with a brief pedagogical overview of DFT. In mathematics a function $f(x)$ is a rule that associates a number with each value of the variable x for which the function is defined. In a similar way a functional $F(f)$ is a rule that associates a number with each function f.

In 1964 Pierre Hohenberg and Walter Kohn showed that the Schrödinger equation, formulated as an equation of a N-electron wave function of 3N variables, could be reformulated as an equation of the electron density with only three variables [64]. In other words DFT attempts to calculate E_0 and other ground state molecular properties from the ground state electron density $\rho_0(\mathbf{r})$ (usually written $n(\mathbf{r})$ in DFT), without having to find the molecular wave function. However the Hohenberg–Kohn theorem [64] does not tell us how to calculate the E_0 from $\rho_0(\mathbf{r})$ nor does it tell us how to find $\rho_0(\mathbf{r})$ without first finding the wave function.

An important step forward applying DFT to real systems was taken in 1965 when Kohn and Sham published the Kohn and Sham (KS) equations [65] derived from the Hohenberg Kohn theorem [64]. The KS equations [65]

$$\left[-\frac{\nabla^2}{2} + \upsilon_{\mathrm{KS}}[n](\mathbf{r}) \right] \varphi_i(\mathbf{r}) = \varepsilon_i \varphi_i(\mathbf{r})$$

recast the Schrödinger equation problem of interacting electrons moving in an external potential into a problem of non interacting electrons moving in an effective potential. The notation $\upsilon_{\mathrm{KS}}[n]$ means that the Kohn–Sham potential, υ_{KS}, has a functional dependence on $n(\mathbf{r})$, the electronic density, which is defined in terms of the Kohn–Sham wave-functions by

$$n(\mathbf{r}) = \sum_i^{\mathrm{occ}} |\phi_i(\mathbf{r})|^2$$

The potential υ_{xc} is defined as the sum of the external potential (normally the potential generated by the nuclei), the Hartree term and the exchange and correlation (xc) potential: $\upsilon_{\mathrm{KS}}[n](\mathbf{r}) = \upsilon_{\mathrm{ext}}(\mathbf{r}) + \upsilon_{\mathrm{Hartree}}[n](\mathbf{r}) + \upsilon_{\mathrm{xc}}[n](\mathbf{r})$

The external potential is typically a sum of nuclear potentials centered at the atomic positions,

$$\upsilon_{\mathrm{ext}}(\mathbf{r}) = \sum_\alpha \upsilon_\alpha(\mathbf{r} - \mathbf{R}_\alpha)$$

υ_α is the Coulomb attraction between the bare nucleus and the electrons, $\upsilon_\alpha(\mathbf{r}) = -Z_\alpha/r$, where Z_α is the nuclear charge. In some cases the use of the Coulomb potential renders the calculation unfeasible, and one has to resort to pseudo-potentials. $\upsilon_{\mathrm{Hartree}}[n](\mathbf{r})$ is the Hartree potential given by

$$\upsilon_{\mathrm{Hartree}}(\mathbf{r}) = \int d^3 r' \frac{n(\mathbf{r}')}{|\mathbf{r} - \mathbf{r}'|}$$

Finally, $\upsilon_{\mathrm{xc}}[n](\mathbf{r})$ is the exchange (xc) potential, which is formally defined through the functional derivative of the exchange-correlation energy, E_{xc},

$$\upsilon_{\mathrm{xc}}(\mathbf{r}) = \frac{\delta E_{\mathrm{XC}}}{\delta n(\mathbf{r})}$$

A vast number of approximate xc functionals, f_{xc}, have appeared in the literature over the past 40 years. The origin of this variety of density functionals (DFs) is due to the approximation, the consequences of which have different effects on chemical problems. This is why the DFT method became "semi-empirical" over the years because as the range of applications increases new functionals had to be developed for handling new problems. We will present and analyze the most common DFs in the next section.

In Kohn–Sham theory, the total energy is written as

$$E_{\mathrm{DFT}} = -\sum_i^{\mathrm{occ}} \int d^3 \phi_i^*(\mathbf{r}) \frac{\nabla^2}{2} \phi_i(\mathbf{r}) + \int d^3 r \upsilon_{\mathrm{ext}} n(r)$$

$$+ \frac{1}{2} \int d^3 r \int d^3 r' \frac{n(\mathbf{r})n(\mathbf{r}')}{|\mathbf{r} - \mathbf{r}'|} + E_{\mathrm{xc}}$$

The terms in this equation are the non-interacting (Kohn–Sham) kinetic energy, the external potential, the Hartree and the E_{xc} energies respectively. Using the KS equation the above equation can be further simplified to the formula implemented in most DFT codes:

$$E_{\mathrm{DFT}} = \sum_i^{\mathrm{occ}} \varepsilon_i - \int d^3 r \left[\frac{1}{2} \upsilon_{\mathrm{Hartree}}(\mathbf{r}) + \upsilon_{\mathrm{xc}}(\mathbf{r}) \right] n(\mathbf{r}) + E_{\mathrm{xc}}$$

When performing geometry optimization or nuclear dynamics, one needs to add to the total energy a repulsive Coulomb term that accounts for the interactions between the ions:

$$E_{\mathrm{nn}} = \sum_{\alpha, \beta} \frac{Z_\alpha Z_\beta}{|\mathbf{R}_\alpha - \mathbf{R}_\beta|}$$

For more details on the foundations of DFT we redirect the reader to some publications [66–68]. Moreover, a recent survey of chemically relevant concepts and principles extracted from DFT, the so-called conceptual DFT, by Geerlings et al. [69] and by Ayers and co-workers [70,71], are very informative.

2.3. DFT tools available (DFT machinery)

In DFT the wave function is constructed in a different way than in Hartree–Fock (HF) and the resulting orbitals are often referred to as "Kohn–Sham" orbitals (KS orbitals). The KS orbitals appear to be as robust as HF orbitals for qualitative interpretation and rationalization of molecular properties. The chief difference between the SCF and KS-DFT approaches lay in the exchange-correlation, f_{xc}, DFs. If the exact form for the f_{xc} DF were known, the KS-DFT approach would give the exact energy. The development of a vast number of DFs resulted in one of the most accurate and fastest approaches for the calculation of electronic structure and properties of large molecular systems. The key to this remarkable success of DFT was its capability to include a large part of the dynamic electron correlation via the exchange-correlation DF, which allowed one to obtain the accuracy in the evaluation of molecular properties comparable with sophisticated ab initio methods but with computational efforts similar to the ordinary HF method. The development of DFT is oriented on the improvement of exchange-correlation DFs to describe energetics and molecular structure more accurately within the framework of the Kohn–Sham method. However, the huge number of developed DFs to date, with various strengths and weaknesses, depending on molecular systems and electronic properties studied, shows that DFT still suffers from several flaws and that the quest for finding a functional, which comes close to the "true one", is still ongoing [72]. No universal DF is available so far in any algorithm to accurately describe a given electron density [63,73,74]. One may classify the DFs into six major groups: local density approximation (LDA), generalized gradient approximation (GGA), meta-GGA, hybrid DFs, double-hybrid DFs, and range-separated DFs.

2.3.1. LDA DFs

The first step toward the exact f_{xc} was the local density approximation (LDA) [75] where only the electron at a point in the system is used for determining this point's contribution to the total E_{xc} of the system. Hohenberg and Kohn showed that, when density differentiates slowly with position in space, the exchange-correlation energy is given by equation,

$$E_{xc}^{LDA}[n] = \int d^3 r n(\mathbf{r}) \varepsilon_{xc}(n(\mathbf{r}))$$

where ε_{xc} is the exchange and correlation energy per particle of a uniform electron gas of density $n(\mathbf{r})$. The LDA uses the exchange-correlation energy of the homogeneous electron gas, evaluated from the charge density at the point $\mathbf{r}$ under consideration. Effectively at $\mathbf{r}$, $n = n(\mathbf{r})$ and E_{xc} is equal to the exchange-correlation energy for the electron-gas system which has a homogeneous charge density n. This is valid if the inhomogeneity of $n(\mathbf{r})$ is small, but the main approximation of LDA is that this is applied even if the inhomogeneity is large. The generalization of LDA that allows different spatial orbital for electrons with opposite spin is known as Local Spin Density Approximation (LSDA) [71]. LSDA gives better results than the LDA for open-shell molecules and molecular geometries near dissociation as it deals separately with the electron density $n^\alpha(\mathbf{r})$ due to the spin-α electrons and the electron density $n^\beta(\mathbf{r})$ due to the spin-β electrons. So the exchange correlation functional is now written as shown in equation,

$$E_{xc}^{LSDA}[n^\alpha, n^\beta] = \int d^3 r n(\mathbf{r}) \varepsilon_{xc}(n^\alpha(\mathbf{r}), n^\beta(\mathbf{r}))$$

LSDA works surprisingly well for calculating molecular geometries, vibrational frequencies and dipole moments even for transition-metal compounds. However the molecular atomization energies calculated with LSDA are not very accurate. For more accurate results functionals that go beyond LSDA are needed.

2.3.2. GGA DFs

Attempts to determine why the LDA and LSDA worked so well led to an enhanced approximate functional, the so called generalized gradient approximation. LDA and LSDA are based on the homogeneous electron gas model which is appropriate for a system where the density varies slowly with position. The integrand in E_{xc}^{LDA} is a functional of only the density and the integrand in E_{xc}^{LSDA} is a function of $n^\alpha(\mathbf{r})$ and $n^\beta(\mathbf{r})$. Functions that go beyond the LDA and LSDA in order to give more accurate results need to correct the LSDA for the variation of electron density with position. The generalized gradient approximation [76–79] functionals do this by including the gradients of $n^\alpha(\mathbf{r})$ and $n^\beta(\mathbf{r})$ in the integrand. This means that the functional is some function of the spin densities plus their gradient as shown in equation,

$$E_{xc}^{GGA}[n^\alpha, n^\beta] = \int d^3 r \varepsilon_X^{GGA}(n^\alpha(r), n^\beta(r), \nabla n^\alpha(r), \nabla n^\beta(r))$$

Gradient corrected functionals are often called "nonlocal" functionals because some nonlocal effects are incorporated for determining a point's contribution to the total exchange correlation energy. Total exchange correlation energy in GGA is split into exchange and correlation parts which are modeled separately. The gradient corrected functionals provided improved accuracy for molecular systems but more steps toward the exact f_{xc}'s were yet to be made.

2.3.3. Meta-GGA DFs

The meta-GGA DFs depend on electron density $n(\mathbf{r})$, its gradient $\nabla n(\mathbf{r})$ and also on the Laplacian of the density $\nabla^2 n(\mathbf{r})$ and/or the orbital kinetic energy (semi-local interactions) [80,81]. So the exchange correlation functional is now written as shown in equation,

$$E_{xc}^{MGGA}[n^\alpha, n^\beta] = \int d^3 r \varepsilon_X^{MGGA}(n^\alpha(\mathbf{r}), n^\beta(\mathbf{r}), \nabla n^\alpha(\mathbf{r}), \nabla n^\beta(\mathbf{r}),$$
$$\nabla^2 n^\alpha(\mathbf{r}), \nabla^2 n^\beta(\mathbf{r}), \tau^\alpha, \tau^\beta)$$

The Laplacians of the density $\nabla^2 n(\mathbf{r})$ seem like the more natural next step, since they appear in the fourth-order gradient expansion, but the Kohn–Sham orbital kinetic energy densities

$$\tau_\sigma(\mathbf{r}) = \frac{1}{2} \sum_i^{occ} |\nabla \phi_{i\sigma}(\mathbf{r})|^2$$

which appear in the Taylor expansion of the exchange hole density about |r'-r|=0, are also functionals of the density and permits the satisfaction of more constrains than the Laplacian do.

2.3.4. Hybrid DFs

In 1993 Becke [82] proposed to mix GGA functionals with exact exchange resulting in a hybrid functional. The exact exchange is sometimes denoted E_X^{HF} since it uses a Hartree Fock definition of E_X. Ever since the proposal of Becke many hybrid functionals have been constructed. Some of them are made from scratch while some others are based on previous constructed hybrid functionals and can be seen more like hybrid functional improvements. The hybrid DFs introduced by Becke [82] are based on the adiabatic connection fluctuation-dissipation theorem (ACFD). The hybrid DFs are functionals that substitute part of the exchange functional with

non-local exchange calculated by HF theory, E_{HF-X} [82–84].

$$E_{xc}^{HGGA}[n] = \int d^3r \varepsilon_X^{MGGA}(n(\mathbf{r}), \nabla n(\mathbf{r})) + \alpha_X E_{HF-X}$$
$$+ \int \varepsilon_C^{HGGA}(n(\mathbf{r}), \nabla n(\mathbf{r}))$$

There are numerous hybrid functionals in use nowadays. This is a sign of the DFT method's utility but also a serious indication that none of the hybrid functionals is suitable for all systems. Another problem that arises from the previous remark is that as the complexity of systems investigated by DFT grows, the task of choosing the right functional becomes increasingly difficult. Actually the best way to evaluate every new DFT functional is to perform systematic comparisons between the results calculated with various functionals and the best theoretical estimations and experimental results. Although hybrid functionals give generally accurate results further improvements in the accuracy of DFT calculations have to be made and better functionals need to be developed.

2.3.5. Double hybrid DFs

The double hybrid DFs are functionals that substitute also part of the correlation energy with correlation energy calculated by ab initio methods (e.g. MP2) [85].

$$E_{xc}^{HGGA}[n] = \int d^3r \varepsilon_X^{HGGA}(n(\mathbf{r}), \nabla n(\mathbf{r})) + \alpha_X E_{HF-X} + (1 - \alpha_C)$$
$$\int \varepsilon_C^{HGGA}(n(\mathbf{r}), \nabla n(\mathbf{r})) + \alpha_C E_{MP2}$$

In other words the double hybrid DFs combine a standard hybrid-GGA DFT calculation with a second order perturbative treatment based on KS orbitals, thus introducing non-local correlation effects (information about virtual KS orbitals).

2.3.6. Range-separated DFs

The range-separated DFs are based on the separation of the electron-electron interaction into two parts, one long-range and the other short-range and treating the two parts with different functionals. One way to construct range-separated DFs is to mix long-range HF with short-range DFs, thus forming simple long-range corrected DFs and another way is to construct screened functionals utilizing short-range HF and long-range DFs [86–95].

Perdew and co-workers [96] offered a prescription for the design and selection of density functional approximations, while Ramos and co-workers [97] provided an overall picture of the level of performance of the plethora of currently available DFs for each chemical property. Very recently Cohen, Mori-Sánchez and Yang [98] provided an account of some of the challenges for DFT arising in the construction of approximations to the exact exchange-correlation, f_{xc}, density functional. The hierarchy of approximations to f_{xc} has been formulated as a Jacob's ladder (Scheme 1) connecting the earth (Hartree theory) to the heaven (chemical accuracy) [96].

Currently, computational chemists have a wide variety of density functionals at their disposal, ranging from LDA to double-hybrid DFs. Some of the most common DFs you may come across are compiled in Table 1.

2.4. General comments on the most popular density functionals

The choice of the DF is the only limitation of the DFT method. At the present time, there is no systematic way of choosing the DF and the most popular ones in the literature have been derived by careful comparison with experiment. It should be emphasized that great care has to be exercised in choosing the DF to calculate spin states in transition metal complexes [127–131].

The local or semilocal DFs on the first three rungs of the Jacob's ladder perform well as well as they do for molecules because there is a strong cancelation between the full nonlocalities of exchange and correlation. However LDA is not recommended for chemistry.

BLYP one of the earliest GGA functionals is usually inferior to BP86 and PBE, but predicts too long bonds.

BP86 predicts excellent geometries and vibrational frequencies and performs often well in spectroscopic investigations.

PBE a nonempirical GGA is very popular in physics. PBE performs equally well as BP86.

PW91 one of the older GGA DFs predicts exchange couplings with excellent accuracy.

OLYP is a GGA DF that violates the uniform electron gas limit, performs well for molecules.

B97-D3 is the most accurate GGA functional followed by **BLYP-D3**

TPSS is the only nonempirical meta-GGA functional. TPSS performs better than PBE for the prediction of atomization energies for molecules and surface energies for solids.

B3LYP the most widely used hybrid functional in quantum chemistry (de facto standard in chemistry) showed excellent
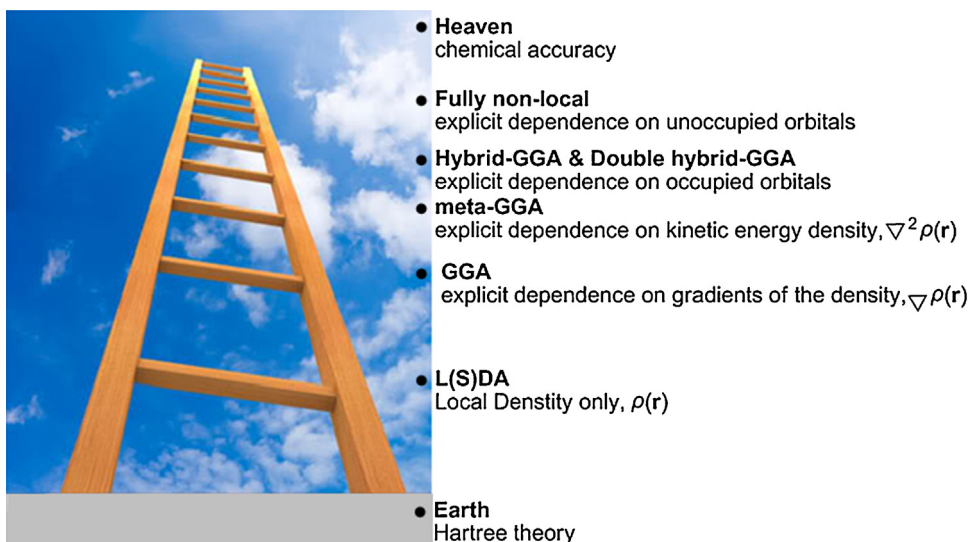
Scheme 1. Hierarchy of approximations to f_{xc} formulated as a Jacob's ladder.

Table 1
Most common density functionals (DFs) in DFT model chemistry.

Density functional	Exchange functional	Correlation functional	Refs.
L(S)DA			
S-VWN3	Slater	VWN no 3	[75]
S-VWN5	Slater	VWN no 5	[75]
S-PWL	Slater	PW local	[75]
GGA			
BP86	B88	P86	[76,78]
BPW91	B88	PW91	[78]
BPBE	B88	PBE	[78,99]
BLYP	B88	LYP	[78,100]
XLYP	B88 + PW91	LYP	[78,79,83,101]
OLYP	OptX	LYP	[83,101,102]
PBE	PBE	PBE	[99]
mPWLYP	mPW	LYP	[83,103]
mPWPW91	mPW	PW91	[103]
HCTC	HCTC	HCTC	[104]
meta-GGA			
BB95	B88	B95	[78,81]
mPWB95	mPW	B95	[81,103]
mPWKCIS	mPW	Krieger-Chen-Iafrate-Savin	[103,105,106]
M06-L	Truhlar-Zhao	Truhlar-Zhao	[107]
PBEKCIS	PBE	Krieger-Chen-Iafrate-Savin	[99,105,108]
TPSS	TPSS	TPSS	[109]
TPSSCIS	TPSS	Krieger-Chen-Iafrate-Savin	[105,109]
tHCTC	HCTC	HCTC	[102]
VSXC	Van Vourhis-Scuseria	Van Vourhis-Scuseria	[110]
Hybrid- and double hybrid-GGA			
B1B95	B88	B95	[78,81]
B3LYP	B88	Lee–Yang–Parr	[78,81,83]
B3P86	B88	P86	[76,78,83]
B3PW91	B88	PW31	[78,83]
B97-2	B97-2	B97-2	[104]
BB1K	B88	B95	[78,81,111]
BMK	BMK	BMK	[112]
M05	Minnesota	Minnesota (28% HF exchange)	[113]
M05-2X	Minnesota	Minnesota (56% HF exchange)	[114]
M06-2X	Minnesota	Minnesota (54% HF exchange)	[115]
M08-HX	Minnesota	Minnesota (52.23% HF exchange)	[116]
MPW1K	mPW91	PW91	[103]
MN12-SX	Minnesota	Minnesota (screened exchange)	[117]
O3LYP	OptX	Lee–Yang–Parr	[83,102,118]
PBE0	PBE	PBE	[99]
TPSSh	TPSS	TPSS	[109]
X3LYP	B88 + PW91	Lee–Yang–Parr	[78,79,83,119]
Range-separated DFs			
B97XD	Modified B97 exchange DF for short-range interactions		[120]
ω-B97XD	Parametrized DF including 100% long-range exact exchange		[120]
B2PLYP-D	$E_{xc} = (1 - c_x)E_{x,B88} + c_x E_{x,HF} + (1 - c_c)E_{c,LYP} + c_c E_{c,MP2}(c_x = 0.53, c_x = 0.27)$		[121]
CAM-B3LYP	Coulomb-attenuating method-B3LYP		[88]
DFT-D3	Dispersion-corrected conventional DFs		[122]
DSD-BLYP	$E_{xc} = (1 - c_x)E_{x,B88} + c_x E_{x,HF} + (1 - c_c)E_{c,LYP} + c_0 E_c{}^0{}_{,MP2} + c_s E_c{}^s{}_{,MP2} + E_D$		[123]
LC-ωPBE	Long-range-corrected hybrid PBE exchange functional		[124]
DFT-dDXDM	Density-dependent dispersion corrected conventional DFs		[125]
DFT-dDsC	Density-dependent energy corrected conventional DFs		[126]

performance in the calculation of structures, energies and properties of molecules.

PBE0 is a widely used hybrid functional competitive with B3LYP. PBE0 provides excellent accuracy.

Minnesota functionals (M05-2X, M06-2X etc.) perform well but are not robust.

B2PLYP the first member of the double hybrid class of functionals has been proven excellent for energies and geometries. Generally all double hybrid DFs outperform all other functionals and are more accurate than MP2 or SCS-MP2 [122].

B97XD, ω-B97XD these long-range corrected DFs are generally somewhat superior in overall performance on a test set of data, which includes atomization energies, reaction energies, non-covalent interaction energies, equilibrium geometries, and a charge-transfer excited state compared with the results obtained by conventional DFT methods [120].

CAM-B3LYP predicts energetic quantities to the accuracy of B3LYP, while for charge transfer energies it is possible to achieve chemical accuracy (0.1 eV). This functional is a hybrid functional with improved long-range properties [88].

DFT-D3 developed by Grimme predict reaction energies and activation barriers with higher accuracy (errors reduced by up to 1.5 kcal mol⁻¹) than those predicted by conventional DFT methods (errors of 6–8 kcal mol⁻¹). Even double hybrid methods, whose mean errors are much smaller (about 3 kcal mol⁻¹), can be improved by over 0.5 kcal mol⁻¹ with the inclusion of the "-D3" correction.

DSD-BLYP This is a Dispersion Corrected, Spin-component scaled Double Hybrid with remarkable performance offering significantly enhanced robustness for systems with significant non-dynamical correlation.

LC-ωPBE This long-range-corrected hybrid is remarkably accurate for a broad range of molecular properties, such as thermochemistry, barrier heights of chemical reactions, bond lengths, and most notably, description of processes involving long-range charge transfer.

DFT-dDXDM the dependent dispersion corrected DF, improves dramatically the performance of popular functionals (e.g., PBE-dDXDM or B3LYP-dDXDM) for a set of 145 systems featuring both inter- and intramolecular interactions [125].

DFT-dDsC The density-dependent energy correction, dDsC, presented herein, is constructed from dispersion coefficients computed on the basis of a generalized gradient approximation to Becke and Johnson's exchange-hole dipole moment formalism [126]. The comprehensive benchmarking on 341 diverse reaction energies divided into 18 illustrative test sets validates the robust performance and general accuracy of dDsC for describing various intra- and intermolecular interactions. The DFT-dDsC is especially valuable for modeling redox reactions and charged species in general.

2.5. Solvent effects on molecular properties of coordination compounds

The continuing development of implicit solvent models for predicting solvation free energies (ΔG_{solv}) is driven by their importance in better understanding and estimating reaction rates, mechanisms, and equilibria in solution, and fundamental aspects of biological and medicinal chemistry [132,133].

When a real molecule passes from the gas phase into solution its structure will relax to permit greater charge separation (electronic polarization). The solute also will polarize the solvent (electric polarization). The energy terms associated with these polarizations are generally referred to as electronic, nuclear, and polarization, and are primarily a function of the bulk dielectric. Other effects exist that are more specifically associated with the first solvation shell, namely the cavitation energy (making a "hole" in the solvent for the solute) the attractive dispersion forces between the solute and solvent molecules and the local structural changes in the solvent, such as changes in the extent of hydrogen bonding.

The current methods for solvation modeling generally follow one of two approaches. The first involves the explicit construction of a solvent shell, consisting of anywhere from several dozen to several hundred solvent molecules, about the solute. This supermolecular system serves as a basis for simulations from which thermodynamic data related to solvation can be extracted. By contrast, the explicit representation of the solvent leads automatically to inclusion of the cavitation, dispersion and solvent structural effects. The main alternative to these simulation procedures replaces the explicit solvent molecules with a continuum having the appropriate bulk dielectric constant. More recently, continuum approaches have been developed that use a generalized Born formalism for the interaction of atomic partial charges with a surrounding dielectric. In principle, the atom centered monopoles generate all of the multipoles required to represent the electronic distribution. Neither of these continuum approaches as described attempts to take account of the energetic effects in the cavitation, dispersion and solvent structural terms, thus focusing on a different set of contributions to solvation than the molecular dynamics methods.

The most widely used class of implicit solvent models in quantum chemistry is the continuum self-consistent reaction field solvation models (SCRF), better known as "polarized continuum models" (PCMs) [134]. The PCM family of solvation models including the conductor-like PCM (C-PCM), the dielectric version of PCM (D-PCM), the integral-equation-formalism versions of PCM (IEF-PCM), isodensity PCM (IPCM), and self-consistent isodensity PCM (SCI-PCM) are physically motivated models that are directly interwoven into the system's Hamiltonian, and can thus be used to explore the effects of solvation on a variety of chemical and physical properties. These include solution-phase geometries, vibrational frequencies, electronic excitation energies, and more.

The conductor-like screening model (COSMO) is a continuum solvation model, where the solute molecule forms a cavity within the dielectric continuum of permittivity that represents the solvent. The charge distribution of the solute polarizes the dielectric medium. The response of the medium is described by the generation of screening charges on the cavity surface. The COSMO solvation model, a variant of the dielectric continuum solvation models, has become very popular due to its algorithmic simplicity, numerical stability, and its great insensitivity with respect to outlying charge errors. The advanced model COSMO-RS [135], i.e., COSMO for realistic solvation, is a statistical thermodynamics theory based on COSMO polarization charge densities, which overcomes many of the limitations and theoretical shortcomings of dielectric continuum models. PCM models are usually more accurate than the COSMO models.

Another continuum solvation model based on the quantum mechanical charge density of a solute molecule interacting with a continuum description of the solvent was reported by Marenich, Cramer, and Truhlar [136]. The model called SMD is a universal solvation model, where "universal" denotes its applicability to any charged or uncharged solute in any solvent or liquid medium for which a few key descriptors are known (in particular, dielectric constant, refractive index, bulk surface tension, and acidity and basicity parameters). Recently the Minnesota group presented a self-consistent state-specific vertical excitation model called VEM, for electronic excitation in solution [137]. The authors used various implicit solvation models combined with time-dependent density functional theory (TD-DFT) that starts with a SCF step for optimizing the orbitals of a reference state, i.e. the Kohn–Sham or generalized Kohn–Sham determinant that represents the ground state density in DFT.

Finally, as a rule of thumb when studying coordination compounds in the condensed phase, exploring reaction mechanisms, estimating reaction rates, investigating equilibria in solution and simulating electronic (absorption and emission), vibrational and nuclear magnetic resonance (NMR) spectra some model of the environment must be included in DFT calculations at least employing the PCM or COSMO solvation models. Examples of the influence of solvent effects on the properties and chemical reactivity of coordination compounds will be given in Section 3.

2.6. Relativistic effects on molecular properties of coordination compounds

When dealing with molecules containing heavy atoms, it is a well known fact that relativity has to be considered in order to obtain an accurate description of molecular properties. Within the relativistic framework, the electronic structure of a molecule is described by the approximate relativistic Dirac–Coulomb Hamiltonian, which for n-electron molecular systems containing N nuclei, under the Born–Oppenheimer approximation is usually taken to be (in atomic units)

$$H_{\text{DC}} = \sum_{i=1}^{n} h_{\text{D}}(i) + \sum_{i=1}^{n} \sum_{j>1}^{n} \frac{1}{r_{ij}}$$

$h_{\text{D}}(i)$ is the four-component one-electron Dirac operator written in Hartree atomic units (a.u.) as

$$h_{\text{D}}(i) = c\boldsymbol{\alpha} \bullet \mathbf{p}_i + (\boldsymbol{\beta} - 1)c^2 - \sum_{A=1}^{N} \frac{Z_A}{R_{iA}}$$

where c denotes the speed of light in vacuum (137.0359998 a.u.), $\boldsymbol{\alpha}$ is a three-vector whose components are (4×4) the Dirac matrices made up from Pauli spin matrices $\sigma = (\sigma_x, \sigma_y, \sigma_z)$ on the off-diagonal, $\mathbf{p}_i$ the linear momentum operator, $\boldsymbol{\beta}$ is a diagonal (4×4) matrix with $(1, 1, -1, -1)$ as elements on the diagonal and a shift in the energy by the rest energy c^2 (in a.u.) in order to match the non-relativistic energy scale. The Coulomb attraction between the electrons and the nuclei A is finally accounted for by the last term. References to recent review articles [138,139] are provided for a non-specialist to be familiarized with the state of the art relativistic quantum chemistry methods. From a practical point of view among the all-electron methods that have found widespread use are the methods based on the Zero Order Regular Approximation (ZORA) and Douglas–Kroll–Hess (DKH) Hamiltonians [140].

The ZORA Hamiltonian [141,142] is written as,

$$H_{ZORA} = V + \frac{1}{2}(\boldsymbol{\sigma} \cdot \boldsymbol{p})K(\boldsymbol{\sigma} \cdot \boldsymbol{p}) = V + \frac{1}{2}(\boldsymbol{p} \cdot K\boldsymbol{p}) + \frac{i}{2}\boldsymbol{\sigma} \cdot [\boldsymbol{p}K \times \boldsymbol{p}]$$

where

$$K = \frac{2c^2}{2c^2 - V} = \frac{1}{1 - V/(2c^2)}$$

Douglas–Kroll–Hess theory (DKH, DKH1, DKH2,...) accomplishes a decoupling of positive- and negative-energy eigenstates of the Dirac one-electron Hamiltonian by an expansion in the external potential. At low orders, this expansion already converges and provides efficient relativistic Hamiltonians to be used in routine quantum chemical calculations.

Both ZORA and DKH (DKH, DKH1, DKH2,...) model chemistries furnish sufficiently accurate relativistic effects in heavy element compounds, thus allowing for meaningful calculations of many spectroscopic, structural, and energetic properties could be implemented in most of the computational packages with widespread use (ABINIT, ADF, DIRAC, Gaussian, MOLPRO, NWChem, ORCA, TURBOMOLE, etc.).

2.7. General instructions for successful application of DFT in coordination chemistry

Quantum Chemistry programs (software packages) offer a vast number of choices of DFs, and selecting a suitable DF can be a daunting task. To select a DF you should:

- Search the literature for calculations on similar coordination compounds and properties and use a DF that is well tested for your domain of application.
- Compare your "candidate" DFs by searching in the publications that describe their development for their strengths and weaknesses, especially with respect to the types of calculations you want to run.
- Empirical dispersion corrections for these DFs are frequently essential for correct chemistry.
- Find out how the candidate DFs perform with different basis sets (DFs with empirical parameters sometimes produce better results with "medium" basis sets if they have been parameterized to do so).
- Choose with care the basis set of the highest possible quality for the system of interest. For heavy metals use relativistic ECPs, such as LANL2DZ or SDD, while for the rest of the atoms use at least the 6-31G(d) basis set. Def-2 type basis sets for heavy metals are strongly recommended. For anionic species diffuse functions must be added as well. Scalar relativistic corrections (ZORA, DKH, ...) are more rigorous than ECPs and spin-free calculations are not much more expensive.
- Run some "calibration" calculations on some model molecules similar to the ones you want to study where you can compare the accuracy of possible DFs and basis sets to decide which combination is best for your "production" calculations.
- Perform single point calculations at a higher level of theory, such as CCSD(T) with a larger basis set, on the optimized geometry, when it is computationally possible with the computational resources available to get more realistic energetic data.
- Construct with care a model with computationally convenient size to represent the "real" big-sized systems or use the hybrid QM/MM method.
- When studying systems in solution, use a solvation model (PCM, COSMO or SMD).
- Compute spectra, such as IR, NMR, Raman, UV–vis, PES etc., which can help in identifying new compounds and predict their reactivity. Relativistic and solvent effects are crucial for accurate prediction of the spectra. Simulate the absorption and emission spectra of coordination compounds under study employing TD-DFT methodology using DFs that account well for the excited states (e.g. PBE0 or CAM-B3LYP). Reviews on TD-DFT benchmarks recently reported by Adamo and Jacquemin [143] and by Laurent and Jacquemin [144] could help to pave the way to choose the "right" DF for your TD-DFT calculations.
- For mechanistic studies determine the structures and energies of reactants, transition states, intermediates and products. Include solvation in studies of reaction mechanisms involving charged species to correctly predict the energetic reaction profile. Investigate the factors controlling the reactivity and selectivity of the particular reaction and create rules for the design of new compounds.
- Investigate the electronic and bonding properties of the compounds under study by applying charge density and energy partitioning schemes and natural bond orbital (NBO) population analysis techniques.

3. Selected most recent successful applications of DFT in coordination chemistry

We now consider applications of DFT of particular interest to coordination chemistry that have appeared in the recent literature. The number of papers reporting DFT calculations has recently increased in the field of coordination chemistry (exploring reaction mechanisms, studying electronic states and structures, simulating among others the electronic, vibrational and NMR spectra). It is our wish to comment here on the more recent developments in the area, presenting a few case examples of successful applications of DFT methods in coordination chemistry. In particular we selected recent papers that best illustrate the promise of DFT in a number of very active areas of coordination chemistry.

3.1. Mechanistic studies – catalysis

The application of electronic structure calculation methods to reactions of transition metal compounds has earlier been reviewed [1,30,31,4,145,27,146]. Moreover, some books have also been devoted to computational organometallic chemistry [147] and the theoretical aspects of homogeneous catalysis [148].

Treatment of the reactions with quantum chemical methods involves calculations of geometries and energetics of reactants, intermediates, transition states, and products. The essential features of a chemical reaction mechanism are contained in the minimum energy path(s) – the path(s) of steepest descent connecting reactants and products via transition states. The minimum energy path is also referred to as an intrinsic reaction coordinate (IRC). Reactants (R) and products (P) correspond with energy minima, whereas transition states (TSs) linking products to reactants usually correspond with first-order saddle points on the potential energy surface (PES).

Exploring reaction mechanisms by DFT methods one has to calculate the *geometric* and *energetic reaction profiles*. In most existing computational suite packages the search algorithms generally look for energetically optimized intermediate (IM) and transition state structures which are closest to the initial input structures and they cannot automatically locate the global minimum structures on the PES along the minimum energy reaction pathway. The location of the saddle points corresponding to TSs on the PES is more difficult than finding local minima corresponding to reactants, intermediates and products. Generally, if a program is given a molecular structure and searches for an TS, it will first compute the Hessian matrix. The nuclei are then moved in a manner, which increases the energy in directions corresponding to negative eigenvalues of the Hessian and decreases energy where there are positive eigenvalues (quasi-Newton technique). Another very useful technique is to start from the reactant and product structures and applying the quadratic synchronous transit methods (OST2 and QST3). In QST2 the software package will require the user to provide as input the structures of reactants and products, while in QST3 a possible transition structure is also required. The QST techniques fail for multi-step reactions, but it can be used individually for each step. TS structures can also be obtained by following the reaction path from the equilibrium geometry to the TS, the so-called eigenvalue-following (EF). Nonetheless, the aforementioned saddle point searches sometimes fail to converge, or they converge to critical points that are minima, thereby more robust algorithms are still needed. Once the TS has been obtained, it may be useful to consider the exact path that lead back to the reactants and forward to the products using the IRC method, thus verifying that the TS is a true TS. Finally, the nature of the stationary points on the PES along the reaction pathway results from the harmonic vibrational analysis implemented in the calculations and are characterized by the number of imaginary frequencies (NImag): NImag = 0 for minima, and NImag = 1 for TSs.

To confirm whether the theoretically predicted reaction mechanism is correct or not, the estimated activation energies should be correlated with experimental data, if such data are available. In the case of a shortage of experimental data or a poor correlation between experimental and computational data, observation, isolation and characterization of the intermediates located on the calculated PES is a reliable practical method. As a rule of thumb, DFT must be calibrated on the basis of experimentally determined barrier heights and/or very high level and computationally expensive ab initio MO methods.

When studying catalytic cycles it is important to know the turnover frequency (TOF) of the cycle given as the number of cycles (N) per catalyst concentration (C) per time (t):

$$\text{TOF} = \frac{N}{[C]t}$$

The TOF is the traditional measure of the efficiency of the catalyst and is routinely available in experimental chemistry. Recently,

Kozuch and Shaik [149,150] developed the energetic span model, which allows for the calculation of the TOF of catalytic cycles from the computed energy profile. In the energetic span approximation TOF is given as,

$$\text{TOF} \approx \frac{k_B T}{h} e^{-\delta E/RT}$$

where δE, the energetic span, corresponds to the apparent activation energy of the full cycle and is defined as,

$$\delta E = E_{\text{TDTS}} - E_{\text{TDI}} \quad \text{if TDTS appears after TDI}$$

$$\delta E = E_{\text{TDTS}} - E_{\text{TDI}} \quad \text{if TDTS appears before TDI}$$

The TOF-determining transition state (TDTS) and the TOF determining intermediate (TDI) correspond with the transition state and intermediate respectively, that maximize the energetic span within the cyclic constrains and thereby gauge the kinetics of the cycle. The versatility of the energetic span model was demonstrated with several catalytic cycles [150].

3.1.1. Catalytic reactions catalyzed by group 8 (Fe, Ru, Os) metal complexes

The mechanism of the iron-catalyzed cross-coupling of aryl electrophiles with alkyl Grignard reagents was studied by a combination of GC reaction progress monitoring, Hammett competition experiments, and DFT calculations [151,152]. DFT calculations were performed to calculate the reaction free energy for all single steps in the proposed catalytic cycles (Fig. 1) and shine some light on the mechanism, since kinetic studies were unable to differentiate between the two paths. The authors correctly used the dispersion – corrected B3LYP-D3 functional for dispersion interactions although insignificant for small model systems have a strong impact for actual experimental systems.

The reaction proceeds via a rate-limiting oxidative addition of the aryl halide to a Fe^I complex formed in situ. A rapid thermoneutral transmetalation from a Grignard reagent could occur either before or after the oxidative addition followed by an exergonic reductive elimination of the resulting alkyl aryl Fe^{III} complex, thus closing the catalytic cycle. The active catalyst was predicted to be an Fe(I) species which has a spin state of S = 3/2, even though the precatalytic Fe(III) salts have a high spin state (S = 5/2). The spin change occurs after the first transmetalation, when the strong ligand field of the aryl group raises the energy of one *d*-orbital, inducing electron pairing [152].

Olefin metathesis has become a powerful ubiquitous reaction in organic synthesis since it allows for the formation of new carbon–carbon double bonds even in the presence of functional groups. The olefin metathesis reaction catalyzed by Ru-based complexes (the well-known Grubbs-type catalysts) has been widely studied from a computational point of view, since a long-standing controversy has been whether the mechanism involves an isomerization from the initial *trans*-dichloro Ru to a *cis*-dichloro Ru
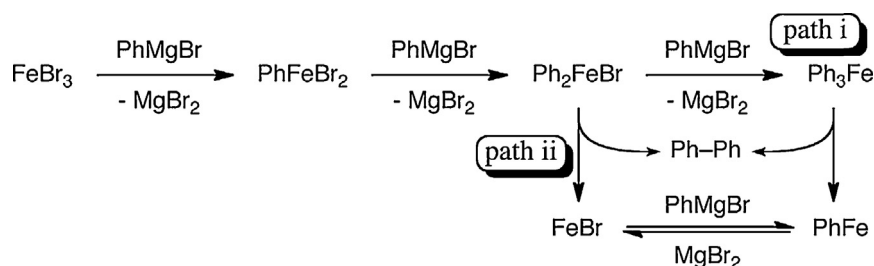

Fig. 1. Suggested reaction mechanisms for the iron-catalyzed homocoupling of aryl Grignard reagents. Ligands are excluded.
Figure reproduced with permission from Ref. [152]. Copyright 2013: Elsevier B.V.

geometry leading to a side-on mechanism proposed by Grubbs to rationalize the observed reactivity and selectivity, but without direct experimental evidence. An overview of computational studies done of the metal carbene complexes tested in homogeneous alkene metathesis as catalysts after the discovery of the Chauvin mechanism [153] (Scheme 2) was recently presented [154]. The Chauvin's mechanism involves four steps: (i) coordination of an alkene (**B**) to the metal of the metal carbene (**A**), (ii) a $[2 \times 2]$-cycloaddition between the metal carbene and the alkene to form a metallacyclobutane intermediate (**C**), (iii) the breaking of the metallacyclobutane intermediate to form a carbene and an alkene (**D**), (iv) the replacement of the coordinated alkene with a new alkene to restart the cycle (**F**).

We now consider the most recent computational studies, employing DFT methods, of the homogeneous alkene metathesis catalyzed by Grubbs-type catalysts.

The mechanism and origins of Z-selectivity in olefin metathesis with chelated Ru catalysts were explored using density functional theory [155]. Olefin metathesis with chelated Ru catalysts occurs via a side-bound mechanism in which the olefin attacks *cis* to the NHC and *trans* to the chelating adamantyl group. The preference for the side-bound mechanism is attributed to a combination of steric and electronic effects of the chelated catalyst. The side-bound mechanism enables steric repulsions between the substituents on the olefin and the N-substituent on the N-heterocyclic carbene ligand (NHC) that lead to highly selective formation of the (Z)-olefin products.

Density functional theory calculations accounting for dispersion, thermochemical, and continuum solvent effects have been applied by Minenkov et al. [156] to study the metathesis of ethyl vinyl ether as mediated by ruthenium catalysts $L(PCy_3)(X)_2Ru=CHPh$ ($L = PCy_3$, IMes (1,3-dimesitylimidazol-2-ylidene), H_2IMes (1,3-dimesityl-4,5-dihydroimidazol-2-ylidene); $X = Cl, Br, I$) in toluene. The computational approach has been validated against experimental data, which give acceptable accuracy even for weakly bound transition states of phosphine and olefin dissociation and association. From the active 14-electron complex, the barriers to both phosphine association (at a rate proportional to k_{-1}) and olefin binding (k_2) involve contributions from entropy and solute–solvent interactions.

Mechanistic details of the catalytic cycle of the water-oxidation catalyzed by $[Ru^{II}(damp)(bpy)(H_2O)]^{2+}$ complex have been studied both experimentally and using DFT (M06-L) and CASSCF/CASPT2 calculations [157]. A detailed DFT analysis of the catalytic cycle (Fig. 2) predicts that the O—O bond formation step proceeding via a water nucleophilic attack mechanism to be rate-determining and to take place for a formal Ru(V)=O species.

### 3.1.2. Catalytic reactions catalyzed by group 9 (Co, Rh, Ir) metal complexes

Cobalt complexes of the type $[CpCoL_2]$ ($L = CO$, PR_3, alkenes) have been used extensively for the cyclotrimerization of alkynes and they are probably the most studied catalysts for these transformations. An overview of the computational studies used to explore the mechanisms of the CpCo- and CpRuCl-catalyzed cyclotrimerization of alkynes and the $[2 + 2 + 2]$ cycloaddition of alkynes to alkenes was recently presented by Varela and Saá [158].

The Co-catalyzed $[2 + 2 + 2]$ cyclotrimerization reactions are assisted by the synergic application of microwave and solid supporting reagents. Recently a computational study employing DFT (B3LYP) methods was carried out to clarify the reaction mechanism, the catalytic cycle and explain the effect of microwave irradiation in these reactions [159]. Both the singlet and triplet PESs were computed taking into account all possible crossings. The favored mechanism takes place by means of an intramolecular metal-assisted $[4 + 2]$ cycloaddition. In the proposed mechanism the first step involves coordination of the dipropargylamine to the cobalt complex and spontaneous oxidative coupling yielding the key cobaltacyclopentadiene intermediate, which relaxes to the triplet ground state. Next the cobaltacyclopentadiene intermediate evolves through the more kinetically favorable path, by coordination of benzonitrile, intramolecular metal-assisted $[4 + 2]$ cycloaddition, intersystem crossing to the triplet state, and dissociation to the final product. Microwave irradiation promotes this reaction with high activation energy. The support exerts a beneficial entropic effect allowing the aligned disposition of both triple bonds and avoiding the formation of byproducts through di- and trimerization of the diyne starting material.

DFT calculations have been performed by Yang et al. [160] to study the mechanism of the Co-catalyzed ligand controlled hydroarylation of styrenes. By examining the detailed mechanism they found that in the C—H activation and C—C reductive elimination steps, styrene is not coordinated to the Co center. In the insertion step, styrene is inserted into the Co—H bond rather than the Co—C bond. Furthermore, the rate- and regiodetermining step is that of C—C reductive elimination.

The hydroformylation of terminal alkenes is one of the most important industrial processes, which relies on homogeneous catalysis yielding a variety of oxo products [161]. A variety of Rh complexes have been used as catalysts. The generally
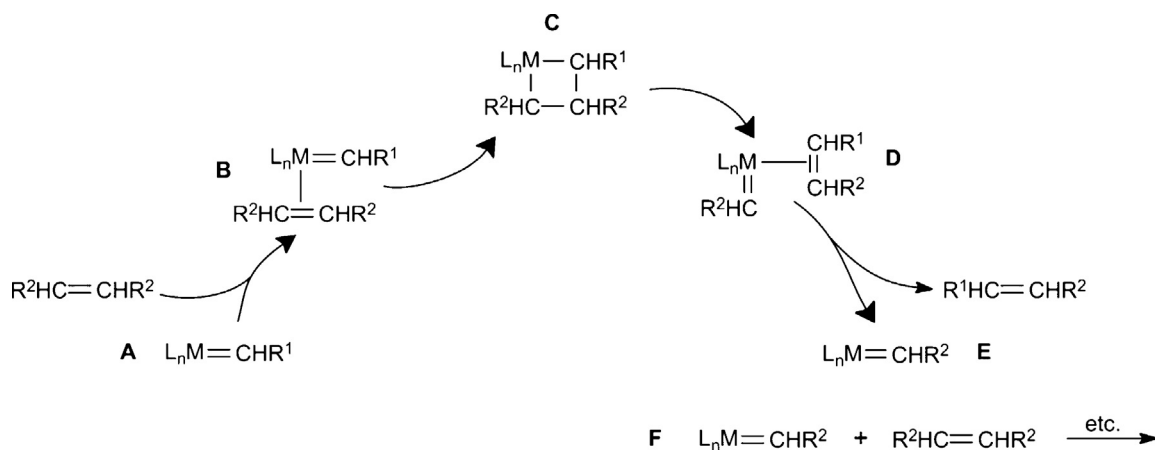
Scheme 2. Reaction scheme of the alkene metathesis metal carbene mechanism.
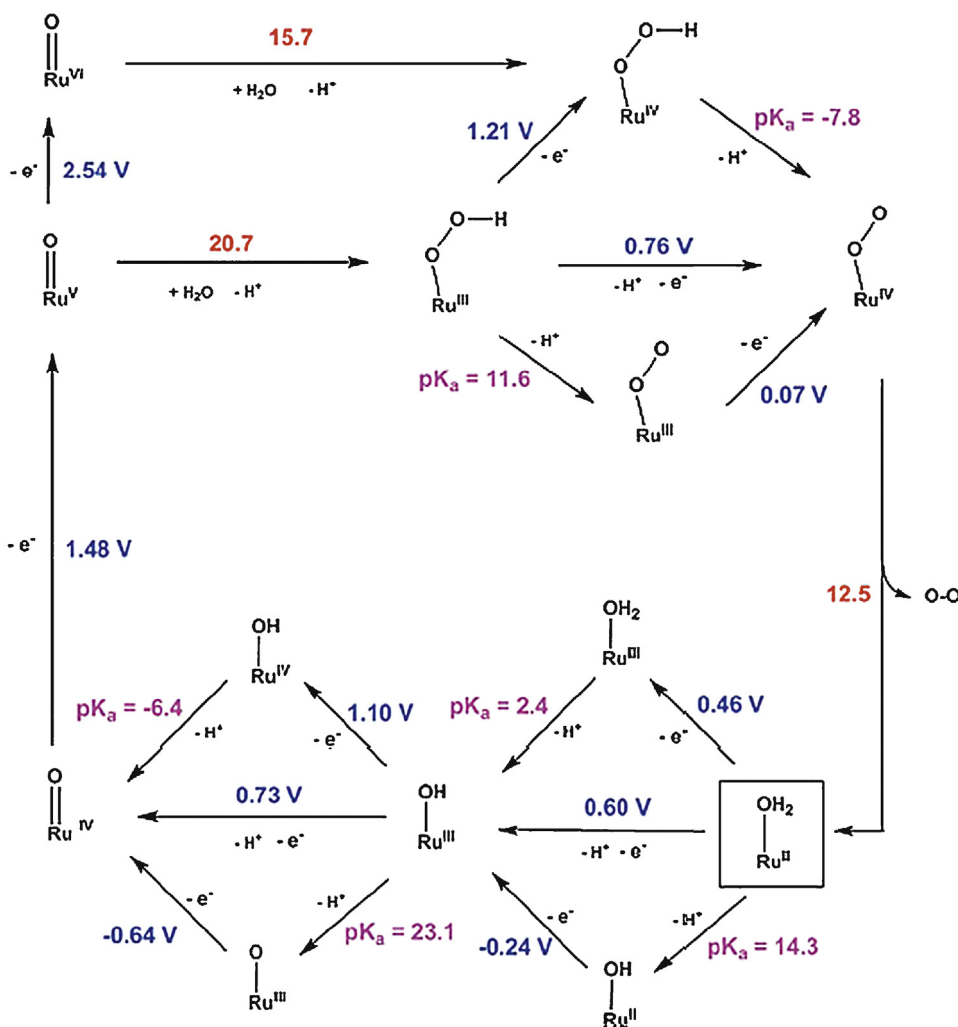Figure reproduced with permission from Ref. [153]. Copyright 2013: Elsevier B.V.

Fig. 2. Catalytic cycle for $[Ru^{II}(damp)(bpy)(OH_2)]^{2+}$ predicted from M06-L calculations; free energy values in kcal mol^{-1}, electrochemical potentials in volts, and pK_a values in log units.

Figure reproduced with permission from Ref. [157]. Copyright 2012: The Royal Society of Chemistry.

accepted mechanism [162] for hydroformylation of alkenes catalyzed by rhodium complexes with general formula $[HRh(L)_2(CO)]$ (L = phosphine, diphosphine or diphosphite ligands) consists of seven steps: (i) CO dissociation, (ii) alkene coordination, (iii) hydrometalation, (iv) CO coordination, (v) migratory insertion leading to a rhodium acyl complex, (vi) oxidative addition in the presence of H_2, and (vii) reductive elimination of the product aldehyde and regeneration of the catalyst.

Very recently a comprehensive computational investigation of the catalytic cycle of rhodium-catalyzed hydroformylation with the $[HRh(L)_2(CO)]$ (L = 6-diphenylphosphino-pyridine-(2H)-1-one) was reported by Gellrich and co-workers [163]. Depending on the functionals used (BP86, B3LYP), the results were found to differ strongly. In this context, the complete catalytic cycle was calculated by using highly accurate Coupled-Cluster with Single and Double and Perturbative Triple excitations (CCSD(T)) computations for a PH_3 model ligand. The authors applied an integrated molecular orbital plus molecular orbital (IMOMO) method consisting of CCSD(T) as high level and DFT as low-level method. The IMOMO calculations yielded excellent agreement with the experimental results for the two popular DFT functionals (BP86 and B3LYP) used. The reliability of the calculations was further tested by the energetic span model and the predicted activation barrier was in excellent agreement with the experimentally determined activation barrier.

The mechanism of the anti-Markovnikov oxidative amination of styrene with piperidine catalyzed by cationic rhodium(I) complexes containing P,O-functionalised arylphosphine ligands has been investigated by spectroscopic and computational means under stoichiometric and catalytic conditions [164]. The catalytic cycle has been studied by a series of DFT calculations disclosing the most plausible intermediates. In addition, the transition states of the key steps have been found and characterized. The catalytic cycle takes place at two stages. The first stage leads to the oxidative amination of styrene and is followed a concomitant styrene hydrogenation stage, which closes the cycle. The most energetically demanding step of the styrene amination stage is the amido insertion into the coordinated styrene ligand.

The current status of knowledge on asymmetric iridium-catalyzed direct hydrogenations of acyclic and cyclic imines has recently been reviewed [165]. The proposed mechanisms for iridium-catalyzed direct imine hydrogenations are either the *inner-sphere* mechanisms, which involve coordination of the imine to the metal center during hydrogenation or the *outer-sphere* mechanisms, involving hydrogenation of an unbound imine substrate in the outer shell. However, to our knowledge, for the majority of these systems, the knowledge about the mechanistic details and the selectivity-determining factors evaluated through theoretical modeling are limited. Hopmann and Bayer

[166] provided a comprehensive quantum mechanical study of Ir-(PHOX)-mediated (PHOX = phosphinooxazoline ligand) hydrogenation of both alkene and imine substrates. The computational results support an Ir(III)/Ir(V) reaction cycle, where the orientation of the metal-coordinated alkene substrate determines the stereochemistry of the resulting product. The suggested catalytic cycle involving dissociation of the imine substrate correctly reproduces the stereoselectivity of imine reduction, but indicates that the enantioselectivity should be more sensitive to the reaction conditions and less controllable than the enantioselectivity of alkene hydrogenations.

Theoretical studies on the hydrogenation of carbon dioxide catalyzed by an Ir-PNP complex were performed by Tanaka et al. [167] using DFT methods. The theoretical results explained the experimental observations that the catalytic cycle is dependent on both the strength of the base and hydrogen pressure. Two competing reaction pathways were suggested: either the deprotonative dearomatization step or the hydrogenolysis step as the rate-determining step.

The direct arylation reaction of benzene and various heteroarenes catalyzed by a Ir[III]-based catalyst was investigated by DFT (B3LYP) calculations [168]. The calculations demonstrated that the Ir[III]-catalyzed direct C—H arylation occurs through the concerted metalation-deprotonation (CMD) pathway which accounts for the experimentally observed regioselectivity (Fig. 3).

Tobish [169] reported a computational examination of diverse mechanistic pathways for intramolecular hydroamination of prototype 2,2-dimethyl-4-penten-1-amine by Cp*Ir chloropyrazole (Cp* = pentamethylcyclopentadienyl) in the presence of KO^{t}Bu base with the aid of DFT calculations employing the TPSS and B3LYP-D3 DFs. The proposed mechanistic scenario entails the following three steps: (i) facile, reversible N—C ring closure through nucleophilic anti attack of the amine on the metal coordinated, thus activated, C=C bond, (ii) stepwise protonolytic cleavage of the Ir—C bond in the zwitterionic [Cp*IrPz-alkyl] intermediate via transfer of the proton from the ammonium unit onto iridium and subsequent turnover-limiting reductive cycloamine elimination to involve a high-energy, metastable [Cp*IrPz-hydrido-alkyl] intermediate, (iii) facile cycloamine liberation to regenerate the active catalyst species.

3.1.3. Catalytic reactions catalyzed by group 10 (Ni, Pd, Pt) metal complexes

Transition metal-catalyzed cross-coupling reactions have been used extensively in selective carbon-carbon as well as carbon-heteroatom bond-forming reactions under mild conditions [170]. Due to the multistep nature of these catalytic processes mechanistic details were difficult to acquire from experimental studies and therefore computational studies were crucial for elucidation of the mechanism of these very important and useful reactions in organic synthesis and organometallic chemistry. An account of the research devoted to the elucidation of the reaction mechanism for the Pd-catalyzed C-C cross-coupling reactions using computational methods, mostly DFT methods, was recently reported [171]. Generally, the catalytic cycle of the cross-coupling reactions consist of three main steps: (i) oxidative addition, (ii) transmetallation and (iii) reductive elimination.

A theoretical investigation of the Ni-catalyzed (using the Ni(PCy$_3$)$_2$Cl$_2$ catalyst) selective C—O bond activation in cross-coupling of aryl esters [172] illustrated that the overall catalytic cycle consist of the aforementioned three basic steps. Oxidative addition of Ar—OAr to Ni(0) in the presence of PCy$_3$ ligand proceeds through the monophosphine pathway with a barrier of ca. 23 kcal/mol. Transmetalation, proceeds via a base-assisted mechanism with a barrier of ca. 31 kcal/mol, and reductive elimination is the most facile step in the whole catalytic cycle with a barrier of ca. 14 kcal/mol. The computational results explain the selectivity to activate the stronger Ar—O bond in the cross-coupling processes in line with experimental observation.

The Ni-catalyzed (using the Ni(PCy$_3$)$_2$Cl$_2$ catalyst) Suzuki-Miyaura cross-coupling reactions of aryl O-carbamates and O-sulfamates to furnish biaryls in good to excellent yields have been investigated both experimentally and theoretically [173]. The computational study revealed the full catalytic cycles for these
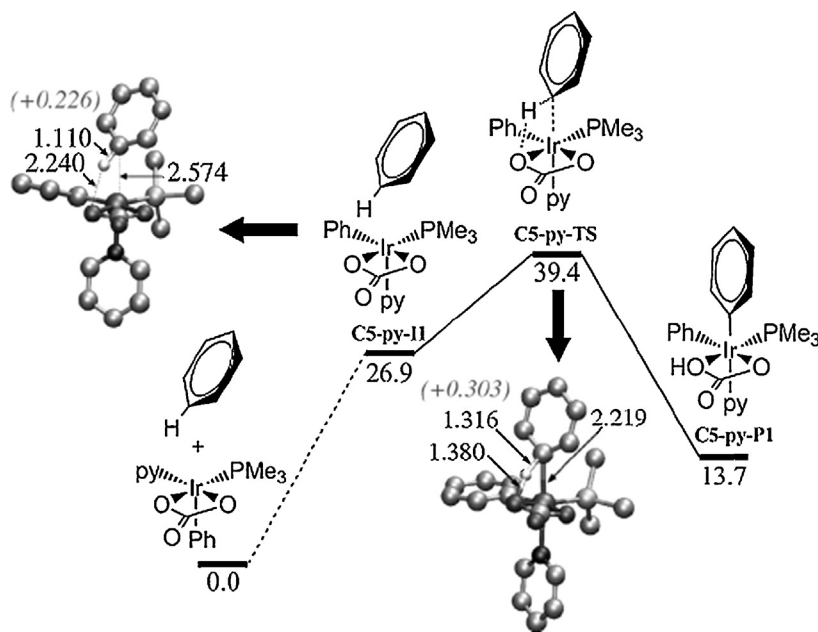
Fig. 3. Gibbs free energy profile (ΔG_s, kcal mol^{-1}) of the CMD reaction pathway for C—H bond cleavage of benzene catalyzed by [Ir(Ph)(PMe$_3$)(py)(CO$_3$)] in toluene solution at 298 K. Hydrogen atoms not involved in the C—H activation step are not shown for clarity. The NPA-derived charges of the ArH fragment in the π-complex intermediate and the CMD TS structure are shown in parenthesis.

Figure reproduced with permission from Ref. [168]. Copyright 2011: Wiley-VCH Verlag GmbH&Co. KGaA, Weinheim.

cross-coupling reactions, thus shedding light on various mechanistic details, rationalizing sulfamate over carbamate higher reactivity, and indicating the role of water in the transition state.

Very recently Steinmetz and Grimme [174] presented the results of an extensive benchmark study of 23 density functionals and wave-function methods for prototype bond activations with four different model catalysts, namely Pd, PdCl$^-$, PdCl$_2$, and Ni. The estimated CCSD(T)/CBS energies based on DFT-optimized geometries served as reference. The PBE0 hybrid functional, together with the atom-pairwise dispersion correction (D3), shows the best performance for the complete set followed by PW6B95-D3, the corresponding double-hybrid functional PWPB95-D3, and B3LYP-D3. The M06 series of DFs with large amounts of Fock exchange perform poorly. Some (meta-)GGAs such as B97-D3 and M06L offer also a good compromise between cost and accuracy and can be recommended for exploratory investigations. The functionals of the M06 series with large amounts of Fock exchange perform poorly. 'Cheap' (meta-)GGAs perform often worse than hybrid functionals, but some (such as B97-D3 and M06L) offer a good compromise between cost and accuracy and can be recommended for exploratory investigations. The addition of the D3 dispersion correction does not affect the activation barriers, but influences significantly the reaction energies. Double-hybrid functionals (DHDFs) with 50–60% of Fock exchange and <30% of perturbative correlation perform best. Based on all results the best 'cost/performance' ratio is offered by hybrid functionals with small amounts of Fock exchange.

The mechanism of the cycloplatination reaction of *cis*-[Pt(Me)$_2$(dmso)(P(*o*-tol)$_3$)] leading to the C,P-cyclometalated compound [Pt{CH$_2$C$_6$H$_4$P(*o*-tolyl)$_2$-κ-*C,P*}(Me)(dmso)] with liberation of methane has been investigated by DFT calculations [175], which confirmed a multistep mechanism. The energy profile given in Fig. 4 shows four reaction steps consisting of (i) reversible dissociation of the dmso ligand to give the T-shaped intermediate [Pt(Me)$_2$(P(*o*-tol)$_3$)], (ii) intramolecular oxidative addition of the C—H bond of a methyl group on the P(*o*-tol)$_3$ ligand to give a pentacoordinate cyclometalated hydride species, (iii) reductive elimination of methane to give a σ-complex, which evolves to the unsaturated 14-electron species, and (iv) fast re-association of the dmso ligand to give the final C,P-cyclometalated square-planar Pt(II) complex (product).
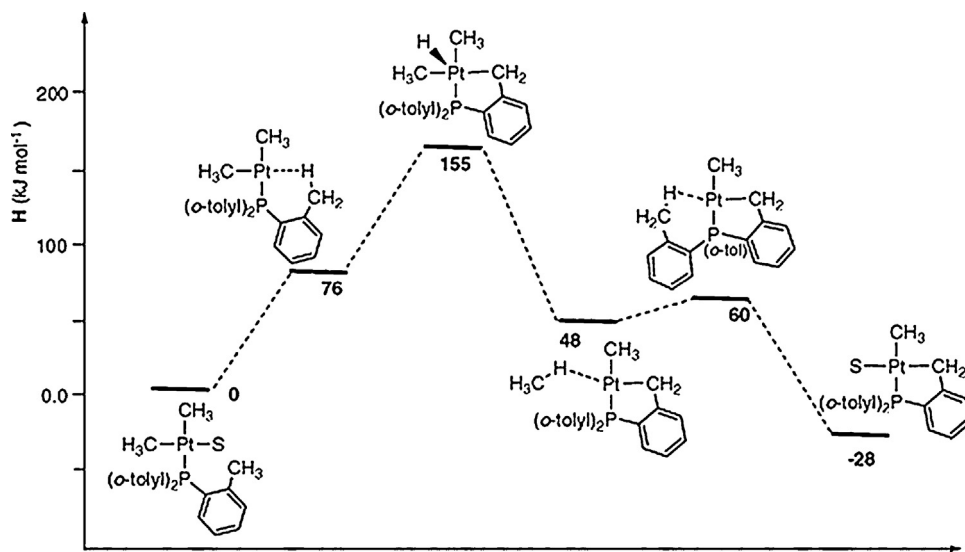
Investigation of the full catalytic cycle for the N—H addition of aniline to ethylene (hydroamination) catalyzed by the PtBr$_2$/Br$^-$ system has been reported by Dub and Poli [176] using DFT calculations on the "real" catalytic system without simplification and with the inclusion of solvation effects in aniline as solvent. The proposed catalytic cycle involves ethylene activation followed by nucleophilic addition of aniline to the coordinated ethylene, intramolecular transfer of the ammonium proton to the metal center to generate a 5-coordinate (16-electron) Pt^{IV}-H intermediate, and final reductive elimination of the PhNHEt product.

Recently Faza and de Lera [177] provided an account of recent developments in the understanding of the mechanisms of gold- and platinum-catalyzed rearrangements of propargylic derivatives. In most of the mechanistic studies the computational method of choice is DFT, allowing some account of electron correlation with a reasonable computational cost. The most popular functional is, by far B3LYP, and the choice of basis sets is usually 6-31G(d) for main group atoms, and an electron core potential (ECP) with its associated basis set for the heavy metals. Among the ECPs used (in order to reduce the computational cost associated with the high number of core electrons in late transition metals and to incorporate in a parametric way some relativistic effects), LANL2DZ is the most common, with some instances of SDD, and BP86 with the LACVP family of basis sets (a combination of Pople's with LANL2DZ effective core basis sets). The choice of this level of theory is usually supported by some general benchmark calculations on sample systems and by the good agreement between the conclusions and predictions from computational studies and the experimental findings at the bench. The first step in many of the noble metal-catalyzed reactions of polyunsaturated systems, and the only available when there are no other external or internal nucleophiles, is the intramolecular cyclopropanation. From these studies some general conclusions that seem to pervade all the mechanistic discussions considered thus far have been extracted.

Experimental and DFT studies in synergy provided mechanistic details for the catalytic conversion of ethylene and benzene to ethylbenzene [178]. The catalytic process involves ethylene coordination and insertion followed by Pt-mediated benzene C—H activation with the latter step, or the C—H coordination step, as the rate limiting step. The DFT calculations were performed at the B3LYP/CEP-31G(5d,7f) level of theory.

Fig. 4. Energetic and geometric reaction profile of the cycloplatination reaction of *cis*-[Pt(Me)$_2$(dmso)(P(*o*-tol)$_3$)] yielding the C,P-cyclometalated compound [Pt{CH$_2$C$_6$H$_4$P(*o*-tolyl)$_2$-κ-*C,P*}(Me)(dmso)], computed at the BP86/TZP level of theory.

Figure reproduced with permission from Ref. [175]. Copyright 2008: The American Chemical Society.

3.1.4. Catalytic reactions catalyzed by group 11 (Cu, Ag, Au) metal complexes

Copper-based catalysts have been known for more than one century and served well for C—N, C—S, C—O and other bond formation reactions [179]. An overview of the recent advances in the copper-catalyzed dehydrogenative functionalization via a single electron transfer (SET) process achieving C—C, C—N, C—O, C—halogen atoms, C—P, and N—N bond formation was very recently presented by Berg and Straub [180]. Many of these catalytic systems were developed based upon detailed mechanistic studies by means of kinetic measurements and DFT calculations. However, the current mechanistic understanding of these transformations and of the complex interplay between catalyst, ligands, solvents, additives, and substrates remains in its infancy.

Very recently Jiménez-Osés et al. [181] reported the results of a synergistic experimental and theoretical study on the copper-catalyzed C—H insertion of diazo compounds into cyclic ethers that allowed for the confident elucidation of the stereochemical course of this reaction. For geometry optimization of all stationary points located on the PES the B3LYP/TZVP computational protocol was employed and solvent effects were considered through single-point energy calculations using the SMD solvation model. Furthermore electronic energies were also computed at the B3LYP-D3/6-31G(d) level of theory. The calculations illustrated that the source of the observed stereoselection arises from a balance of stereoelectronic factors in which the repulsive interactions between the ester group and the alkyl/aryl groups of the oxazoline rings, and also the attractive van der Waals interactions between the substrates and the ligand, play crucial roles.

The carboxylation reactions of arylboronate esters with CO_2 catalyzed by (NHC)Cu(I) complexes (NHC = N-heterocyclic carbene) have been studied by means of DFT calculations [182]. The computational results affirmed the basic mechanistic proposal that the first step involves the transmetalation of the aryl group of the boronic ester to the Cu(I) metal center, the second step involves the insertion of CO_2 into the resulting Cu—Ar bond to give a carboxylate complex, and the third step involves the displacement of the carboxylate by the base adduct of the arylboronic ester substrate affording the product ArCOOK, thus completing the catalytic cycle. Insertion of CO_2 into the Cu—Ar bond is the rate-determining step, in which nucleophilic attack of the aryl ligand on the electron-deficient carbon atom of CO_2 leads to the formation of the new C—C bond.

The copper-catalyzed hydrocarboxylation and hydrosilylation reactions among diphenylacetylene, CO_2 and $HSi(OEt)_3$ has been theoretically investigated by means of density functional theoretical calculations [183] with the aim to answer the question why the reaction preferred hydrocarboxylation rather than hydrosilylation. Calculations indicated that in hydrocarboxylation, CO_2 insertion into Cu-C bond of the copper alkenyl complex and the subsequent σ bond metathesis between Cu—O and H—Si (rate-determining step with a barrier of 30.1 kcal/mol) are kinetically feasible under the reaction conditions, consistent with the experimental observations. On the other hand, in hydrosilylation, the σ bond metathesis was found to be kinetically unavailable (activation barrier of 47.4 kcal/mol) in the presence of CO_2. At the same time Fan, Sheong and Lin [184] reported the results of DFT calculations related to the study of the reaction mechanism of copper-catalyzed hydrocarboxylation of alkynes using CO_2 and hydrosilanes. Through the DFT calculations, the authors make the same conclusion with respect to the reason why only hydrocarboxylation of alkynes has been observed experimentally.

Experiments and DFT computations at the B3LYP/def2-SVP level of theory were employed by Mustard et al. [185] to elucidate the complete mechanism and origins of the diastereospecificity of a Cu(I)-catalyzed rearrangement of vinyloxiranes to dihydrofurans.

DFT computations reveal that an unusual, traceless dual transition-metal-mediated process is operative, and the proposed complete detailed catalytic cycle is shown in Fig. 5.

Gold salts and complexes are the most active catalysts for diverse organic transformations, such as the electrophilic activation of alkynes (hydration, hydroxylation, spiroketalisation, hydroamination of alkynes), cyclisation and cycloisomerisation reactions, and the total synthesis of natural products. A critical review of the most recent advances in the field of gold-catalysis in total synthesis was reported by Rudolph and Hasmi [186].

Very recently Vilhelmsen and Hashmi [187] reported a computational study to elucidate the mechanism of the NHC–gold-catalyzed cyclization of 1-ethynyl-2-(phenylethynyl)benzene to form dibenzopentalene. A mechanism for the dibenzopentalene synthesis by dual-gold activation was proposed based on DFT calculations at the B3LYP/cc-pVDZ level, using an additional relativistic effective core potential from the Stuttgart group for gold and correcting all obtained energies by means of the DTF-D3 corrections. The computed energy profile of the catalytic reaction is shown in Fig. 6.

The reaction path, excluding the catalyst-transfer step, has an overall activation energy of 18.9 kcal/mol ($\Delta\Delta G_{D3}^{\neq} = 19.0$ kcal/mol) with the most energetically demanding single step being the initial intramolecular catalyst transfer from a geminal to a non-geminal state TS5 ($\Delta\Delta G^{\neq} = 7.9$ kcal/mol; $\Delta\Delta G_{D3}^{\neq} = 7.1$ kcal/mol) shows the path of the cationic gold moiety across the π system to form the gem-diaurated complex.

The mechanistic and regiochemical aspects of the Au(I)-catalyzed intermolecular hydroalkoxylation of allenes were studied by Paton and Maseras [188] by means of DFT calculations. The most favorable catalytic pathway is the nucleophilic attack of a Au(I)-coordinated allene, which occurs irreversibly (Fig. 7). The predicted kinetic product is at odds with the experiment, however, a further Au(I)-catalyzed interconversion of the regioisomeric allylic ether products can occur. This rearrangement is predicted to be more facile than the initial allene hydroalkoxylation, and resembles the recently discovered Au(I)-catalyzed rearrangement of allylic acetates.

The performance of 32 DFs to describe the homogeneous gold catalysis of propargyl esters has been tested by Rodríguez and coworkers [189]. Due to the lack of accurate experimental or high-level computational data for such complex multistep catalytic reactions with numerous intermediates, data obtained at the CCSD/def2-TZVPP//CCSD/def2-SVP level were used to validate these functionals. The DFT calculations indicated that accurate results for challenging intermediates are only obtained with the last generation of DFs including corrections of the medium- and long-range interactions. Among these, M06 and B2PLYP generally outperform the rest of the hybrid alternatives.

A detailed DFT computational study of the nucleophilic attack of methanol to 1,2-diphenylacetylene assisted by $[(Ph_3P)Au]^+$ catalyst has been carried out by Mazzone et al. [190] to shed light on the mechanistic aspects of such a process. Conclusions are drawn based on DFT calculations that the rate-determining step of the whole process is the addition of a second nucleophile molecule to the formed enol ether to yield the final ketone product, along the pathway that describes the second part of the reaction.

3.2. Electronic and bonding character in coordination chemistry – conceptual DFT

Nowadays DFT can routinely be employed to invent new molecules and explore unknown new bonding modes in transition metal chemistry. To gain insight into the electronic structure and the bonding features of coordination compounds various population analysis methods, charge decomposition analysis (CDA) and
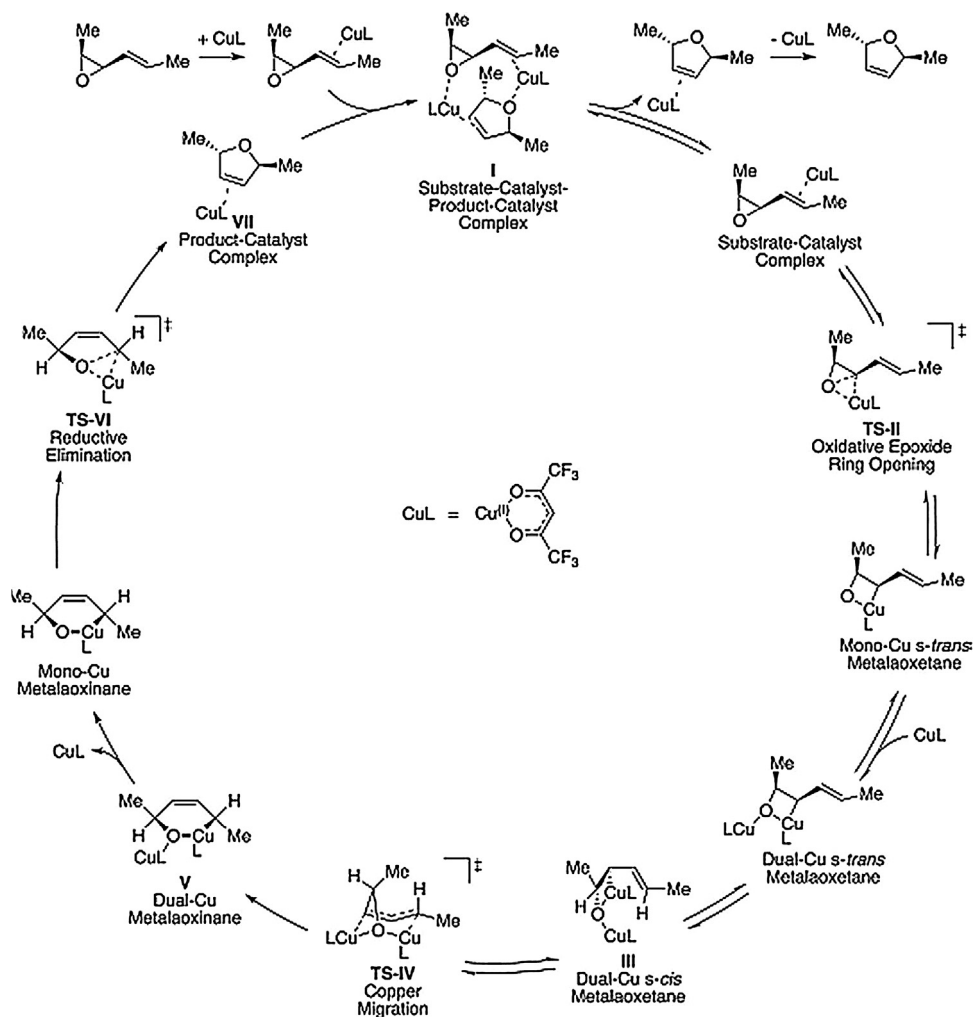
Fig. 5. Complete catalytic cycle for the Cu(I)-catalyzed stereospecific rearrangement of vinyloxiranes to dihydrofurans. Figure reproduced with permission from Ref. [185]. Copyright 2013: The American Chemical Society.

energy decomposition analysis (EDA) methods are employed. Other theoretical tools for analyzing the electronic structure of a molecule are the topological analysis of the electron density distribution, which is also called Atoms in Molecules (AIM) theory, the Electron Localization Function (ELF) and the Reduced Density Gradient (RDG) methods.

There are many population analysis methods dependent on how the electron density is partitioned, we will look at the Mulliken population analysis (MPA), and one that is particularly popular (and combined with a localization procedure) called the Natural Bond Orbital (NBO) analysis.

The MPA is the oldest population method [191] based on orbital wavefunction, supported by almost all quantum chemistry packages. The problem with the Mulliken charge is that it varies significantly as function of the basis set, and does not show any convergence behavior. The MPA is the most common population analysis method, but it is also one of the worst and is used only because it is one of the oldest and simplest.

The NBO method developed by Weinhold and co-workers [192] was designed to give a quantitative interpretation of the electronic structure of a molecule in terms of Lewis structures. The NBO calculations provide natural atomic charges, Wiberg Bond Indices (WBIs), natural electron configurations and bond orbitals. One advantage of the NBO analysis is that the results are quite robust against changing the basis set.

The CDA method as developed by Gernot Frenking et al. [193] is used to study the donor–acceptor interactions of a molecule in terms of two user-specified fragments. The CDA is based on the fragment orbital (FO) formalism, which denotes the molecular orbital (MO) of fragment in its isolated state, i.e. the wave function of a complex L_nM-X is expressed as a linear combination of FOs of the ligand X and the metal-containing fragment L_nM. The FOs contributions to wavefunction of the complex are divided into four parts [193,194]: (i) mixing of the occupied FOs of X and the unoccupied FOs of L_nM that describes the $X \rightarrow ML_n$ donation, (ii) mixing of the unoccupied FOs of X and the occupied FOs of L_nM that describes the $X \leftarrow ML_n$ back-donation, (iii) mixing of the occupied FOs of X and the occupied FOs of L_nM that describes the $X \leftrightarrow ML_n$ polarization and (iv) mixing of the unoccupied FOs of X and the unoccupied FOs of L_nM that describes the rest term Δ, which is a sensitive probe for classification of the compound as a donor–acceptor complex. If the rest term deviates significantly from $\Delta = 0$ the M–X bond corresponds to a normal covalent bond rather than a dative (donor–acceptor) bond.

The EDA method developed by Morokuma [195,196] and later modified by Ziegler and Rauk [197] is a useful tool to estimate the intermolecular interaction energies of metal–ligand systems. Also the separation into the different contributions to this interaction energy gives insight on the nature of the bond. Indeed the interaction energy of a dimer system consisting of monomers A
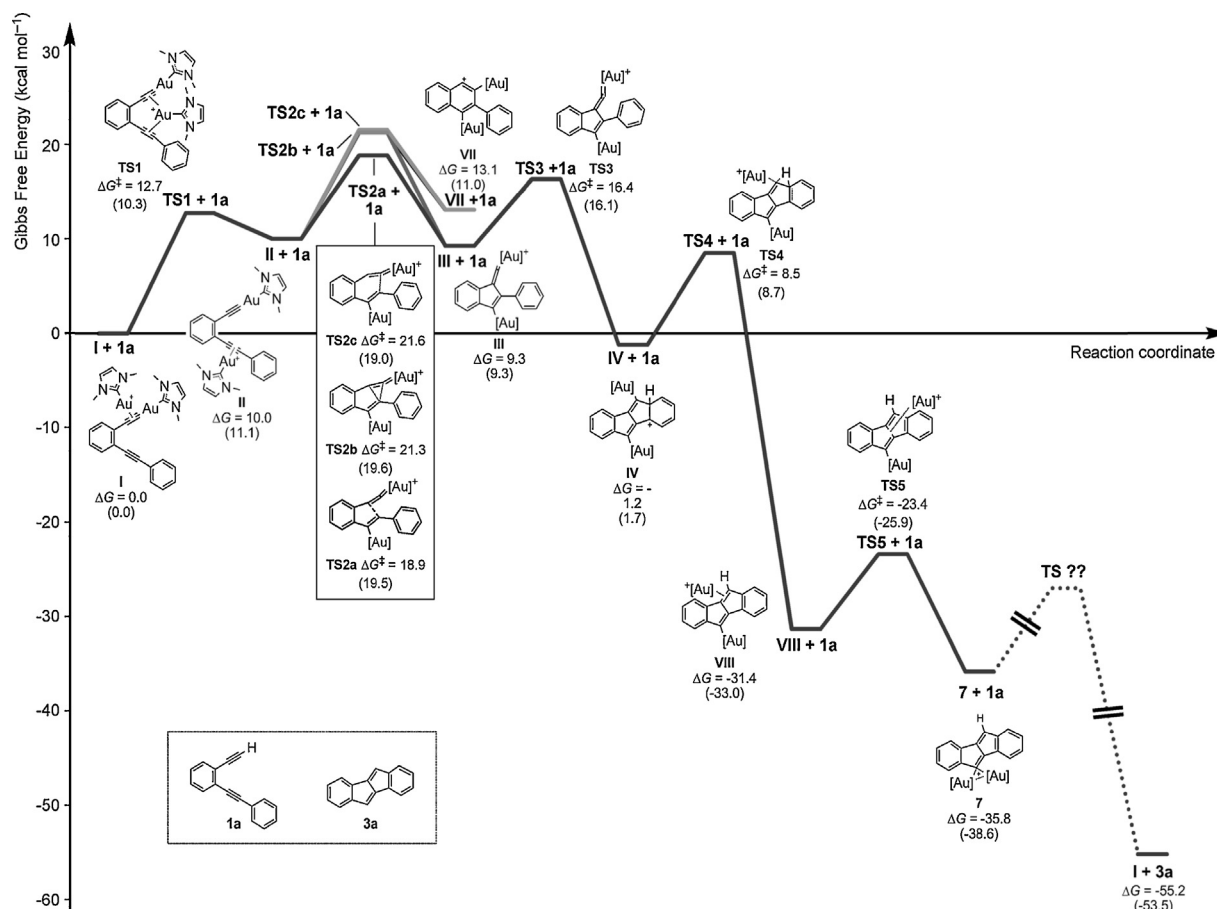
Fig. 6. Full-energy profile of the reaction including the final intermolecular catalyst-transfer step (transition states were not calculated). The parenthesized energies were obtained by D3 correction.

Figure reproduced with permission from Ref. [187]. Copyright 2014: Wiley-VCH Verlag GmbH&Co. KGaA, Weinheim.

and B can be calculated as the sum of different energy terms i.e. electrostatic interaction between the fragments (E_{elec}), exchange-repulsion linked to Pauli's repulsion between parallel spin electrons ($E_{exch-rep}$), the monomer polarization contribution (E_{pol}) due to the relaxation of a given fragment's occupied orbitals within its virtual

orbitals in the field of another fragment, and the charge transfer term (E_{ct}) accounting for donation and back-donation.

$$E_{int} = E_{elec} + E_{exch-rep} + E_{pol} + E_{ct}$$
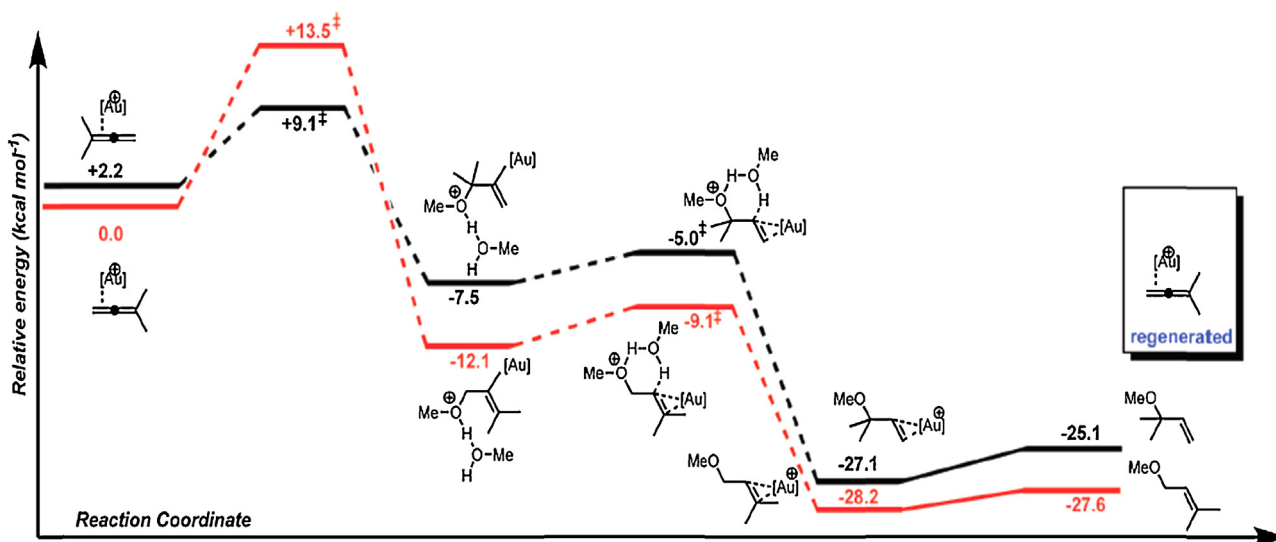
Fig. 7. [NHC]Au(I)-catalyzed hydroalkoxylation reaction coordinate for both regioisomeric pathways. Solution phase energies in kcal mol^{-1} relative to the separated reagents.

Figure reproduced with permission from Ref. [188]. Copyright 2009: The American Chemical Society.

Hopffgarten and Frenking [198] published a review article on the EDA technique demonstrating that EDA is a very powerful method for a qualitative and quantitative analysis of the chemical bond.

The AIM method proposed by Bader [199] is a theoretical tool for analyzing the electronic structure of a molecule based on the topology of the electron density distribution $\rho(\mathbf{r})$. The topoligial analysis of $\rho(\mathbf{r})$, $\nabla\rho(r)$ (gradient field of $\rho(\mathbf{r})$) and $\nabla^2\rho(r)$ (Laplacian of $\rho(\mathbf{r})$) provide information about the electronic structure of a molecule. In topology analysis language, the points at where gradient norm $\nabla\rho(r)$ value is zero (except at infinity) are called critical points (CPs). CPs define the position of the atomic nuclei in the three-dimensional space and can be classified into four types according to how many eigenvalues of Hessian matrix of real space function are negative. When all three eigenvalues of Hessian matrix are negative (local maximum) the position of $(3,-3)$ CP is nearly identical to nuclear positions, hence $(3,-3)$ CP is also called nuclear critical point (NCP). When two eigenvalues of Hessian matrix are negative (second-order saddle point) the $(3,-1)$ CP generally appears between attractive atom pairs and hence is commonly called bond critical point (BCP). Notice that the value of $\rho(\mathbf{r})$ and the sign of $\nabla^2\rho(\mathbf{r})$ are closely related with the bonding strength and bonding mode. For a first-order saddle point (only one eigenvalue of Hessian is negative) the $(3,+1)$ CP generally appears at the center of ring systems and often is called ring critical point (RCP). Finally, for a local minimum (none of eigenvalues of Hessian are negative) the $(3,+3)$ CP generally appears at the center of cage systems and often is called cage critical point (CCP). Cortés-Guzmán and Bader [200] published a review article on the physical understanding of bonding in selected transition metal complexes (Cr, Ir and Ni carbonyl complexes, ferrocene and the anaologous Al^+ and Ge metallocenes) by the AIM and molecular orbital theory methods illustrating the complementarity of the two theories.

The ELF function proposed by Becke and Edgecombe [201] is defined as:

$$\text{ELF}(r) = \frac{1}{1+(D_\sigma/D_\sigma^0)}$$

where D_σ and D_σ^0 represent the curvature of the electron pair density for electrons of identical σ spin (the Fermi hole) for the actual system and a homogeneous electron gas with the same density, respectively.

Within the DFT framework, for a closed-shell system the σ dependence no longer appears on the right-hand site of the equation and the D and D^0 are given as [202,203]:

$$D = \frac{1}{2}\sum_i |\nabla\phi_i(\mathbf{r})|^2 - \frac{1}{8}\frac{|\nabla\rho(\mathbf{r})|^2}{\rho(\mathbf{r})}$$

The ELF is a local measure of the effect of Pauli repulsion on the kinetic energy density and lies within the range of [0,1]. A large ELF value means that electrons are greatly localized, indicating that there is a covalent bond, a lone pair or inner shells of the atom involved.

The RDG is also a very important function for revealing weak interaction region [204] and is defined as:

$$RDG(\mathbf{r}) = \frac{1}{2(3\pi^2)^{1/3}}\frac{|\nabla\rho(\mathbf{r})|}{\rho(\mathbf{r})^{4/3}}$$

A benchmark study of the performance of different versions of the M05, M06, and M08 set of Minnesota DFs for the prediction of the heat of formations (HOFs) and the ionization potentials (IPs) of various first row transition metal compounds has been undertaken by Mishra and co-workers [205]. The eight functionals of M0X family tested were the M05, M05-2X, M06-L, M06, M06-2X, M06-HF, M08-SO, and M08-HX along with the popular Los Alamos National Laboratory2 double-ζ (LANL2DZ) basis set. Totally 54 benchmark systems were taken for HOF calculation, whereas the 47 systems

among these benchmark complexes are chosen for the calculation of IPs because of lack of experimental results on rest of the seven systems. The computed values of HOFs and IPs were compared with the experimental results obtained from the literature. The deviation of these computed values from the actual experimental results was calculated for each eight different M0X functionals to judge their performances in evaluating these properties. The M06-L functional is the best average performer among the M0X series of functionals in row TM complexes, whereas the robust functional M06-HF gives the worst performance in predicting such properties confirming the recommendation of the developers of these functionals that the Minnesota density functionals with high HF exchange should not be used for the TM compounds. Besides M06-L, the M05 and M06 DFs are also to be recommended for the theoretical prediction of these thermochemical parameters for the first row TM complexes.

The performance of several popular DFs (GGA DFs: BLYP, BP86, OPBE, HCTH, PBE, VSXC; hybrid GGA DFs: B3PW91, B3LYP, PBE1PBE, MPW1K, B97-2, B1B95, PBE1KCIS) in predicting the geometrical parameters and energetics of transition metal carbonyl complexes of iron, ruthenium and osmium has been studied by Hirva et al. [206]. The computational results indicated that hybrid DFs best describe the back-bonding ability of the carbonyl ligands and deal with metal–metal bonds. The best general performance was obtained with hybrid functionals B3PW91 and PBE1PBE (PBE0), which therefore provide an efficient tool for solving problems involving large or medium sized transition metal carbonyl compounds.

Bühl et al. [207] assessed optimized and zero-point averaged geometries obtained from DFT computations with various exchange-correlation functionals and basis sets using a set of 41 metal–ligand bond distances in 25 third-row transition-metal complexes, for which precise structural data are known in the gas phase. In the lighter congeners, LSDA affords reasonably accurate geometries of 5d-metal complexes, as it is among the DFs with the lowest mean and standard deviations from experiment. For this set the ranking of some other popular DFs, ordered according to decreasing standard deviation, is BLYP > VSXC > BP86 approximate to BPW91 approximate to TPSS approximate to B3LYP approximate to PBE > TPSSh > B3PW91 approximate to B3P86 approximate to PBE hybrid. In this case hybrid functionals are superior to their nonhybrid variants. Generally, for a combined test set comprising first-, second-, and third-row transition metal complexes, B3P86 and PBE hybrid DFs are indicated to perform best. A remarkably consistent standard deviation of around 2 pm in metal–ligand bond distances is achieved over the entire set of d-block elements.

The forces that control the labile P—C bond in phosphamides and their conjugate acids and related species were studied by NBO methodology within the framework of DFT [208]. Three principal forces, due to electrostatic, covalent, and hyperconjugative interactions, control the structural preferences of the phosphamide ligands and their conjugate acids. Hyperconjugative (anomeric) $n(O) \to \sigma^*(P—C)$ interactions play a key role in tuning the $R(P—C)$ bond length in phosphamides and their conjugate acids. The $n(O) \to \sigma^*–(P—C)$ interactions contribute significantly to the elongation of the $R(P—C)$ bond length. Phosphamides could be stabilized by coordination with early transition-metal ions, such as Ti(IV), but are strongly destabilized by coordination with late-transition-metal ions, such as Ag(I) and Cu(I).

Jensen and co-workers [209] investigated the metal–phosphine bond strengths in transition metal compounds by means of DFT calculations employing the M06 family of DFs as well as GGA and hybrid GGA DFs with and without an empirical term (i.e., DFT-D) accounting for long range dispersion. Electrostatic and nonelectrostatic solvent effects have also been estimated using the polarizable continuum model (PCM), allowing for comparison with experimental data obtained for dissociation reactions in organic solvents.

The GGA and hybrid-GGA DFs grossly underestimate the absolute metal–phosphine bond enthalpies. On the other hand, the recently developed range-separated DFT-based methods (the DFT-D and M06 DFs) dramatically improve upon the situation. The best agreement with experiment is observed for BLYP-D. The authors also stated that the improvements in predicted relative bond enthalpies are less convincing for in several cases the GGA and hybrid-GGA DFs are better at reproducing substitution effects than the DFT-D and M06 methods.

The oxidation half reaction of $[M(CO)_nL_{6-n}]$ complexes ($M = Ru^{2+/3+}, Os^{2+/3+}, Tc^{2+/3+}$; $L = CN^-, Cl^-$, water, CH_3CN, N_2 and CO) were investigated by means of DFT methods [210]. The computed adiabatic energy differences $\Delta E_{adiabatic}$ are linearly correlated with respect to the substitution number n_{CO}, thus supporting the hypothesis of additive ligand effects on the redox potential. The values of the slope of these linear regression curves can act as a ligand specific parameter analogous to Pickett's P_L, Lever's $E_L(L)$, and CEP parameters. Based on these parameters, a computed electrochemical series was constructed.

The molecular and electronic structures, stabilities, and bonding features of a series of metal clusters with the general formulae $[c\text{-}M_3L_n]^+$ and $[c\text{-}M_3(\mu_2\text{-}H)_3L_n]$ (M = Cu, Ag, Au, L = ethylene, acetylene; $n = 1$–3) in their singlet ground states were investigated by DFT, CDA and EDA methods [211]. The upright or in-plane orientation adopted by the η^2-coordinated unsaturated hydrocarbon ligands L in the $[c\text{-}M_3L_n]^+$ and $[c\text{-}M_3(\mu_2\text{-}H)_3L_n]$ complexes respectively is strongly related to the electrophilicity index, ω, of the respective electrophilic $[c\text{-}M_3L_{n-1}]^+$ and $[c\text{-}M_3(\mu_2\text{-}H)_3L_{n-1}]$ fragments. When $\omega > 7$ eV the unsaturated ligands adopt the upright orientation, while for $\omega < 2.95$ eV the in-plane orientation is adopted. CDA and EDA methodologies indicate that acetylene/ethylene are more strongly bound to the "naked" rather than to the hydrido-bridged triangular noble metal clusters, while the $M\text{-}C_2H_2/C_2H_4$ binding interactions are predicted to be predominantly electrostatic rather than covalent.

Takagi, Krapp and Frenking [212] investigated the bonding features of homonuclear and heteronuclear metal–metal multiple bonds in $R_3M\text{-}M'R_3$ (M, M' = Cr, Mo, W; R = Cl, NMe_2) by DFT calculations in conjunction with energy decomposition analysis (EDA). They found that the $M\text{-}M'$ bond strength increases as M and M' become heavier. The strongest bond is predicted for the 5d–5d tungsten complexes $(Me_2N)_3W\text{-}W(NMe_2)_3$ and $Cl_3W\text{-}WCl_3$ with D_e values of 103.6 and 99.8 kcal/mol respectively. The results of the EDA show that the stronger $R_3M\text{-}M'R_3$ bonds for heavier metal atoms can be ascribed to the larger electrostatic interaction caused by effective attraction between the expanding valence orbitals in one metal atom and the more positively charged nucleus in the other metal atom. The metal–metal bonds are characterized as triple bonds where π-bonding is much stronger than σ-bonding.

The electronic structure of the $Ni(PH_3)_2(\eta^2\text{-}CO_2)$ complex, a model compound for the well-known Ni(0) carbon dioxide complexes containing various tertiary phosphane ligands was elucidated using DFT calculations along with domain-averaged Fermi hole (DAFH), AIM, ELF, CDA, and NBO methods [213]. The CO_2 ligand are rather weakly coordinated as the enthalpy of formation from complex $Ni(PH_3)_2$ and CO_2 is -12.7 kcal/mol (-9.5 kcal/mol when counterpoise correction is applied). The coordination of CO_2 ligand to Ni(0) metal center involves the expected π-donation interaction and electron donation from the $C\text{-}O$ σ bond. The back-donation is slightly influenced by the phosphorus atom adjacent to the non-coordinated O of CO_2 as it transfers electron density directly to carbon. This unconventional way of back-donation may also explain the bent character of the Ni–C bond path.

The performance of popular DFT approximations for a variety of Au(I)/Au(III) complexes with unsaturated aliphatic hydrocarbon C_nH_m substrates (ethene, ethyne, and allene) was assessed with

respect to high-level coupled cluster calculations with core-valence correlation and complete basis set (CBS) limit extrapolation as a reference [214]. The tested DFs cover from LDA to GGA and meta-GGA, and to hybrids and double hybrids (LSDA, PBE, M06-L, TPSS, B3LYP, PBE0, M06, M06-2X, TPSSh, B2-PLYP, B2GPPLYP). B2GP-PLYP, PBE0, and B2-PLYP are the best performing DFs for this set of Au-C_nH_m complexes. DFT dispersion correction (DFT-D3), though very helpful for some DFs (e.g., B3LYP and B2-PLYP), does not uniformly improve the results of all DFs.

Comas-Vives and Harvey [215] analyzed the degree of metal-to-ligand backbonding in a range of model transition metal complexes of N-heterocyclic carbenes, through structural and NBO second-order perturbative energy analysis based on DFT calculations. It was concluded that back-bonding is significant in these compounds comparable or indeed larger than that obtained with corresponding phosphane complexes. This is partly due to the very strong σ-donor nature of the ligand, which makes typical metal acceptor centers very electron-rich and hence very apt to undergo backbonding.

An account of the aromaticity in inorganic metallocenes (sandwich compounds of the transition elements with inorganic rings) by Maslowsky Jr. [62] mostly studied by DFT methods is commended to the reader of the present review article.

The nature of bonding in terminal borylene, alylene, and gallylene complexes $[(\eta^5\text{-}C_5H_5)(CO)_3M(ENR_2)]$ (M = V, Nb; E = B, Al, Ga; R = CH_3, SiH_3, CMe_3, $SiMe_3$) was investigated by DFT calculations employing the BP86 DF [216]. The optimized geometry of vanadium borylene complex $[(\eta^5\text{-}C_5H_5)(CO)_3V\{BN(SiMe_3)_2\}]$ is in excellent agreement with the experimentally determined structure. The M—B bonds in the borylene complexes have partial double-bond character, and the B—N bonds are nearly double bonds. On the other hand, the M—E bonds in the alylene and gallylene complexes represent M—E single bonds with a very small M—E π-orbital contribution, and the Al—N and Ga—N bonds in the complexes have partial double-bond character. The contributions of the electrostatic interactions ΔE_{elstat} are significantly larger in all borylene, alylene, and gallylene complexes than the covalent bonding ΔE_{orb}.

Highly accurate estimates of the high-spin/low-spin energy difference ΔE_{HL}^{el} in the high-spin complexes $[Fe(NCH)_6]^{2+}$ and $[Co(NCH)_6]^{2+}$ have been obtained from the results of CCSD(T) calculations extrapolated to the complete basis set limit [217]. These estimates have been used to assess the performances of the CASPT2 method and 30 DFs of the GGA, meta-GGA, global hybrid, RSH, and double-hybrid types. At the DFT level, some of the assessed DFs proved to perform within chemical accuracy (± 350 cm^{-1}) for the spin-state energetics of $[Fe(NCH)_6]^{2+}$, others for that of $[Co(NCH)_6]^{2+}$, but none of them simultaneously for both complexes. A re-parametrized CAM-PBE0 range-separated hybrid DF, led to a DF that performs within chemical accuracy for the spin-state energetics of both complexes.

Bowman and Jakubikova [218] investigated the applicability of the B3LYP functional to accurate prediction of ground state multiplicity of pseudo-octahedral iron complexes. They confirmed the linear relationship between the high-spin/low-spin energy splitting, $\Delta E_{HS/LS}$ ($\Delta E_{HS/LS} = E_{high\text{-}spin} - E_{low\text{-}spin}$), as well as $\Delta H_{HS/LS}$ and $\Delta G_{HS/LS}$, and the amount of exact exchange in the B3LYP DF. Thus $\Delta E_{HS/LS}$ displays a strong dependence on the amount of exact exchange in the DF for coordination complexes of iron with mostly covalent character, such as Fe(II) polypyridines, and B3LYP tends to favor high-spin ground states, while for ionic complexes displays a weaker dependence on c_1, and B3LYP artificially stabilizes the low-spin states. They found that the slope of this dependence strongly correlates with the average change in the metal–ligand bond lengths between the low-spin and high-spin states. It is suggested that a ground state determination of an arbitrary pseudo-octahedral complex of iron could be accomplished by comparing

the calculated energy differences between the singlet and quintet electronic states of an unknown complex to the energy differences of structurally related complexes with a known, experimentally determined ground state.

Wilson and co-workers [219] assessed the applicability, as well as limitations, of the recently developed correlation consistent Composite Approach for transition metals (ccCA-TM) in the predictions of ΔH_f's for an extensive set of 225 first-row transition metal-containing molecules ranging from the monohydrides to larger organometallics such as $Sc(C_5H_5)_3$ and clusters such as $(CrO_3)_3$. Unlike ccCA-TM, two representative DFT methods, B3LYP and M06, perform poorly. This study supports that ccCA-TM algorithm has been demonstrated as an accurate, robust, and widely applicable model chemistry for 3d transition metal-containing species with versatile bonding features.

The structural, electronic, bonding and magnetotropic properties of inclusion compounds formed upon interaction of cerium monoxide, CeO, with buckybowls (quadrannulene, $C_{31}H_{16}$, corannulene, $C_{20}H_{10}$ and sumanene, $C_{21}H_{12}$) as well as with annulenes (cyclobutadiene, C_4H_4, benzene, C_6H_6 and cyclooctatetraene, C_8H_8) have been investigated by DFT calculations at the wB97XD/ANO-RCC(Ce),6-31G**(C,O,H) level [220] of theory. NBO analysis reveal the nature of the metal–ligand bonding consisting of weak covalent interactions involving $\pi \cdots \pi^*$, $\delta \cdots \pi^*$ and $\varphi \cdots \pi^*$ interactions, electrostatic and dispersion forces.

DFT calculations predicted the stability of some exotic aromatic coinage metalated benzenes with general formula $1,3,5$-$C_6H_3M_3$ and C_6M_6 resulted from the trimerization of coinage metal acetylides $MC\equiv CH$ and $MC\equiv CM$ (M = Cu, Ag, Au) [221]. The structural, energetic, magnetotropic, and spectroscopic properties of the metalated benzenes were analyzed and compared to the respective properties of the unsubstituted archetype aromatic benzene molecule.

The coordination affinity of 32 phosphoryl, imino, thiocarbonyl, and carbonyl ligands to the $[Ni(H_2O)_5]^{2+}$ complex was analyzed in terms of geometrical, electronic, and energy parameters calculated by DFT methods [222]. The affinity of the pentaaqua nickel(II) complex for these ligands was analyzed and quantified in terms of interaction enthalpy (ΔH), Gibbs free energy (ΔG_{298}), geometric and electronic parameters of the resultant octahedral complexes. The estimated ΔH and ΔG_{298} values show that the ligand coordination strength increases in the following order: carbonyl < thiocarbonyl < imino < phosphoryl. This coordination strength order was also observed in the analysis of the metal–ligand distances and charges on the ligand atom that interacts with the Ni(II) cation.

Interaction energies and bonding analysis for ML (M = Cu, Ag, Au; L = H_2O, OF_2, OMe_2, NH_3, NF_3, NMe_3, H_2S, SF_2, SMe_2, PH_3, PF_3, PCl_3, PMe_3) complexes were investigated at the CCSD(T) level of theory [223]. Both, electron correlation and relativistic effects are crucial in the bonding of all complexes. Highest binding energies are computed for complexes with Au, followed by Cu and Ag. Computationally less demanding DFT computations at the PBE0/def2-QZVP level provide correct pattern of interaction energies when compared with benchmark CCSD(T) results. The order of stabilities follow the pattern $M \cdots PX_3 > M \cdots NX_3 > M \cdots SX_2 > M \cdots OX_2$. Within $M \cdots PX_3$ complexes the order of binding energies is $M \cdots PMe_3 \gg M \cdots PH_3 > M \cdots PCl_3 > M \cdots PF_3$.

Very recently Chen and Jia [224] in a review article summarized the recent advances in the chemistry of metallabenzenes and metallabenzynes. Both experimental and theoretical studies employing DFT methods suggest that these metallacycles are aromatic molecules that undergo typical reactions of aromatic systems (e.g. electrophilic substitution reaction) as well as organometallic complexes (e.g. formation of cyclopentadienyl or carbene complexes).

The strong intermetallic interactions resulting in a Pt–Pt metal–metal bond and the respective bonding mechanism in the unsaturated trinuclear complex $[(C_6F_5)_2Pt(\mu\text{-}PPh_2)_2Pt(\mu\text{-}PPh_2)_2Pt(PPh_3)]$ were verified by employing a multitude of computational techniques (natural bond order analysis, the Laplacian of the electron density, and localized orbital locator profiles). It was concluded that this complex should be better considered as a Pt^{II}–Pt^{III}–Pt^{I} complex instead of a Pt^{II}–Pt^{II}–Pt^{II} one. The oxidation states of the Pt centers in the complexes were estimated by calculation of the natural charges transferred from the ligands toward the Pt metal centers combined with the natural atomic charges acquired by the Pt centers [225].

The chemical bonding between a copper(I), bipyridine molecules and the decaborate dianion formulated as $[Cu_2(bipy)_2B_{10}H_{10}]$ was investigated by means of DFT calculations at the PBE/PW level for the crystalline state and PBE0/6-311G(d,p) level for the isolated molecules combined with AIM, ELI-D and atomic Hirshfeld surface (AHS) techniques [226]. It was found out, that the Cu – decaborate bonding is characterized with a zone of very flat $\rho(\mathbf{r})$ and very low $\nabla^2\rho(\mathbf{r})$. A clear distinction between 2c–2e and multicenter bonding was performed using intersection of $\rho(\mathbf{r})$ and ELI-D basins. The copper atoms are bonded to borane moiety via a number of weak Cu—B and Cu—H multi-centered bonds.

The structural, bonding, spectroscopic and magnetic response properties of cyclic trinuclear complexes (CTCs) with the general formula c-$M_3(\mu_2$-$X)_3$ (M = Cu, Ag; X = F^-, Cl^-, Br^- or I^-) as well as their adducts with benzene formulated as $[c$-$M_3(\mu_2$-$X)_3]_n(C_6H_6)_m$ ($n, m \leq 2$) were studied by means of DFT and TD-DFT calculations at the B97D/Def2-TZVP level [227]. Special emphasis was given in delineating the controversial nature of the M–X and M–M bonds in the copper(I) and silver(I) halide CTCs as well as their ability to form supramolecular assemblies with benzene acting as π-Lewis acids. To fully understand the c-$M_3(\mu_2$-$X)_3 \cdots C_6H_6$ interactions we applied a multitude of theoretical techniques such as CDA and EDA, NBO population analysis as well as molecular electrostatic potential (MEP) calculations. EDA calculations revealed that the dominant term in the c-$M_3(\mu_2$-$X)_3 \cdots C_6H_6$ interaction arises from dispersion and electrostatic forces while the covalent interactions are predicted to be negligible. CDA calculations illustrated very small charge transfer from C_6H_6 toward the c-$M_3(\mu_2$-$X)_3$ clusters, thus reflecting weak π-base/π-acid interactions which are further corroborated by the respective MEPs and the fact that the total dipole moment vector points to the center of the metallic ring of the c-$M_3(\mu_2$-$X)_3$ cluster. The excitation spectra of all aromatic columnar binary stacks simulated by means of TD-DFT calculations showed strong absorptions in the UV region. The absorption bands are assigned to MLCT, LMCT and MC excitations with participation of the benzene molecule. A blue shift is seen when the first and second benzene molecules are associated with c-$M_3(\mu_2$-$X)_3$ clusters.

In a subsequent paper [228] we studied the molecular and electronic structures, stabilities, bonding features, and magnetotropicity of the columnar binary stacks with general formula $[c$-$Au_3(\mu_2$-$X)_3]_n(L)_m$ (X = halide; L = C_6H_6, C_6F_6, or $B_3N_3H_6$; $n, m \leq 2$) by DFT calculations. In all binary stacks, with only a few exceptions, the plane of the alternating c-$Au_3(\mu_2$-$X)_3$ and L (C_6H_6, C_6F_6, $B_3N_3H_6$) stacking participants adopts an almost parallel face-to-face (**pff**) orientation. The observed trends in the intermolecular distances R in the $[c$-$Au_3(\mu_2$-$X)_3]_n(L)_m$ (X = halide; L = C_6H_6, C_6F_6, or $B_3N_3H_6$; $n, m \leq 2$) columnar binary stacks are explained by the diverse aromatic interactions characterizing the stacks, since the three L ligands and the c-$Au_3(\mu_2$-$X)_3$ CTCs exhibit diverse physical properties such as the zz tensor components of quadrupole moment, Q_{zz}, polarizability, α_{zz}, nucleus-independent chemical shift, $NICS_{zz}(1)$, along with the molecular electrostatic potential,

MEP(0), and surface area (S), which are important determinants of the aromatic interactions. The interplay of electrostatics, charge transfer, and dispersion forces contributing to the interaction energies in the 1:1, 1:2, and 2:1 binary stacks of the c-Au$_3$(μ_2-X)$_3$ (X = F, Cl, Br, I) clusters with benzene, hexafluorobenzene, or borazine was investigated by employing a multitude of theoretical techniques such as CDA, EDA, NBO, as well as MEP calculations. The dominant term in the aromatic (stacking) interactions arises mainly from dispersion and electrostatic forces, while the contribution of covalent interactions is predicted to be small. Important linear correlations of the interaction energy, ΔE_{int}, and its components (ΔE_{disp}, ΔE_{elstat}, ΔE_{orb}, and ΔE_{Pauli}) with the aforementioned calculated physical properties were established. The energy splitting in dimer (ESID) model was employed to estimate the charge transport of electrons and holes between the ligands L and the [c-Au$_3$(μ_2-X)$_3$] clusters in [c-Au$_3$(μ_2-X)$_3$](L) 1:1 binary stacks. Large charge transfer integrals for electron transport, t_{12}^e, are calculated for most of the [c-Au$_3$(μ_2-X)$_3$](L) 1:1 binary stacks, rendering them promising candidates for use as electron channel semiconductors in organic electronics.

3.3. Simulation of the absorption and emission spectra of coordination compounds by TD-DFT

Computation of the spectroscopic and photochemical properties of transition metal complexes is of paramount importance to optimize their performance as light harvesting antennae or photocatalytic centers in photochemical devices, as sensitizers of solar energy conversion, phosphorescent dyes for display applications (organic light emitting diodes, OLED), luminescence-based sensors, active components of electron- or energy-transfer assemblies, molecular devices (molectronics), non-linear optical materials, photoinitiators, triggers of electron transfer in biomolecules, or photocatalysts, providing useful hints to guide molecular design strategies.

Electronic structure calculations of excited states of transition metal complexes have become nowadays a very important complement to spectroscopic techniques. However, the study of ground and excited state properties of coordination compounds using computational methods confront some difficulties arising from the size, the state degeneracies, the dynamical correlation and relativistic effects. Although the most appropriate formalism to describe the ground state and excited state properties of coordination compounds seems to be the multi-configurational (MCSCF) one including relativistic effects, nowadays DFT methods are extensively used to simulate the electronic spectra of transition metal complexes. Among them the most popular is the time-dependent DFT (TD-DFT) approach.

Formal TD-DFT is usually traced back to the classic paper of Runge and Gross [229]. For a given initial state, there is a unique mapping between the evolving density and the time-dependent potential $\upsilon_{ext}(\mathbf{r},t)$. A non-interacting system of the same density may be defined, whose evolution is described by time-dependent Kohn–Sham equations where the orbitals evolve under a time-dependent one-body potential functional $\upsilon_s[n(\mathbf{r}); \Phi(0)](\mathbf{r},t)$:

$$\left[-\frac{\nabla^2}{2} + \upsilon_s[n; \Phi(0)](\mathbf{r}, t) \right] \varphi_i(\mathbf{r}, t) = \varepsilon_i \varphi_i(\mathbf{r}, t)$$

$$n(\mathbf{r}, t) = \sum_{i=1}^{N} |\phi_i(\mathbf{r}, t)|^2$$

$$\upsilon_s[n; \Phi(0)](\mathbf{r}, t)] = \upsilon_{ext}[n; \Psi(0)](\mathbf{r}, t)] + \int d^3r' \frac{n(\mathbf{r}', t)}{|\mathbf{r} - \mathbf{r}'|}$$
$$+ \upsilon_{xc}[n; \Phi(0), \Phi(0)](\mathbf{r}, t)$$

TD-DFT is formally an exact theory, but the actual implementations require the selection of an exchange correlation functional f_{xc} which concentrates the approximations of the model. Information about electronic excited states may be obtained from this theory through the linear response (LR) theory formalism developed by Casida [230–232]. The LR-TD-DFT became nowadays popular for calculating absorption and other spectra of medium- and large-sized molecules. As the number and the diversity of applications of TD-DFT has grown, so too has grown our understanding of the strengths and weaknesses of the approximate functionals commonly used for TD-DFT. In practice, one can state that LR-TD-DFT inherited from all DFT problems but also presents a few specific drawbacks [232]. The LR-TD-DFT works best for low-energy one-electron excitations involving little or no charge transfer and which are not delocalized. Most of the problems attributed to LR-TD-DFT can be resolved by using decent approximations of the DFs. For singly excited states of finite systems asymptotically corrected hybrid DFs with 20–25% of HF exchange lead to the best results. Extensive benchmarking has revealed some systematic errors [232–237] in the calculated excitation energies when use is made of GGA DFs as well as the popular approximate hybrid DFs containing fractions of exact HF exchange. The largest deviations are found for charge transfer transitions or Rydberg transitions [235–237].

Very recently Krykunov, Seth and Ziegler [238] applied the relaxed and self-consistent extension of constricted variational density functional theory (RSCF-CV-DFT) developed earlier by the same authors [239] for the calculation of the lowest charge transfer transitions in the molecular complex X-TCNE between X = benzene and TCNE = tetracyanoethylene. The RSCF-CV-DFT method was evaluated employing a number of different functionals with a fixed percentage (α) of HF exchange ranging from $\alpha = 0$ to $\alpha = 50$ as well as DFs with a length correction that introduces HF exchange for longer interelectronic distances. The evaluation revealed that for the X-TCNE systems all DFs afford a reasonable agreement with experiment in the case of RSCF-CV-DFT whereas only the LC-functionals provide a fair agreement for adiabatic TD-DFT.

An overview of recent progress on TD-DFT with a specific focus on its accuracy and on models able to take into account environmental effects, including complex media was presented by Jacquemin and co-workers [240]. The authors summarized recent benchmarks and defined an average TD-DFT accuracy in reproducing excitation energies when a conventional approach is used. The expected accuracy of TD-DFT is ca. 0.2–0.3 eV, once modern hybrid functionals are applied, but such accuracy can only pertain when the response of the environment to the excited-state of the considered chromophore has to be modeled adequately. For bulk solvent effects, the latest (state-specific) approach of the PCM model allows for accurate evaluation of solvatochromic shifts for both absorption and fluorescence, with corrections with respect to the standard linear-response results that are often non-negligible.

Very recently Laurent and Jacquemin [144] reviewed contributions devoted to the assessment of the performances of exchange-correlation DFs within TD-DFT framework. The authors presented both the different strategies used to assess the DFs and the main results obtained in terms of accuracy. For the majority of properties, states and molecules, pure DFs provide poorer estimates than hybrid DFs. If, despite their inherent limits, one wish to apply pure DFs, meta-GGAs are probably the best choice, especially VSXC and M06-L outperform typical GGA and LDA. In the vertical approximation "traditional" hybrid DFs (e.g., B3LYP, PBE0, or M06) are rather satisfying. For these excited states with strong CT character as well as Rydberg states range-separated (CAM-B3LYP, ωB97-XD) or hybrid DFs (such as M06-2X) are more effective and stand as the best possible choices. Double hybrids, and in particular

B2GPLYP bring significant improvements for excited states having a doubly excited nature.

An overview of DFT and TD-DFT applications to electronic spectroscopy and excited-state properties of d^6 transition metal complexes was presented in a review article by Vlček Jr. and Záliš [241]. Emphasis was given on the effects of the computational procedure on the quality of the results and the type of information obtained. The most accurate CT transition energies and descriptions of excited states of low-valent d^6 metal complexes are obtained when using hybrid DFs and calculating the molecule in the actual solvent.

Garino and Salassa [242] presented an overview on photochemically active transition metal complexes investigated by TD-DFT. In particular, they discussed a representative range of systems studied up to now, which include CO- and NO-releasing inorganic and organometallic complexes, haem and haem-like complexes dissociating small diatomic molecules, photoactive anti-cancer Pt and Ru complexes, Ru polypyridyls and diphosphino Pt derivatives.

In the following we will focus on a few selected recent case applications of TD-DFT in simulating the optical properties of transition metal compounds, aiming to stimulate the interest of inorganic chemists willing to learn new science and to adopt to a somewhat different style he or she is accustomed to, welcoming a combination of theory, computation, and experiment.

Iridium cyclometalated complexes have attracted extensive attention in the recent years because of their potential to achieve a high external quantum efficiency, thus forming the basis for new applications as organic electro-luminescence (OEL) materials in solid-state organic light-emitting diodes (OLEDs) and large-area flexible displays. In particular, iridium complexes, containing large π-conjugated ligands, such as 2-phenylpyridine anions (ppy$^-$) and neutral 2,2′-bipyridines (bpy), have an advantage that their emission wavelength can be tuned from blue to red by the peripheral substitution of phenylpyridines by electron-withdrawing and electron-donating substituents or by replacement of chelating ligands [243–250]. The optical properties of the Ir complexes were investigated by means of TD-DFT calculations employing the popular B3LYP functional. Ortho-metalated iridium compounds exhibit strong phosphorescence, which is used in organic light-emitting diodes (OLEDs) to overcome the efficiency limit imposed by the formation of triplet excitons. Generally, the excited state of the Ir complexes is complicated and contains triplet metal-to-ligand charge transfer (^{3}MLCT), and triplet ligand-to-ligand charge transfer (^{3}LLCT) simultaneously.

Ru(II) polypyridyl complexes have been extensively investigated due to their unique chemical, redox and photophysical properties. Particularly, Ru(II) polypyridyl complexes from a photochemical point of view, show very interesting properties to be exploited in light-based functionalities. Therefore, the number of photophysical studies on Ru(II) polypyridyl complexes has increased considerably during the last 30 years. Ru(II) polypyridyl complexes absorb considerably in the UV–vis region and exhibit long-lived and intense luminescence. Both low-lying singlet and triplet excited states have been theoretically assigned using time-dependent density functional theory (TD-DFT), as singlet and triplet metal-to-ligand charge transfer (^{1}MLCT and ^{3}MLCT, respectively) states. In the following we will focus on a few selected recent publications concerning TD-DFT simulation of the optical properties of ruthenium complexes.

Schulze et al. [251] reported the synthesis of a heteroleptic bis(tridentate) ruthenium(II) complex (RuCNC) of the new 2′,6′-bis(1-mesityl-3-methyl-1,2,3-triazol-4-yl-5-idene)pyridine (CNC) ligand and the parent tpy (tpy = 2,2′:6′,2″-terpyridine). The electronic and optical properties of RuCNC were investigated by experimental and theoretical studies. TD-DFT calculations in the presence of acetonitrile (PCM-TD-B3LYP/6-31G*) were performed
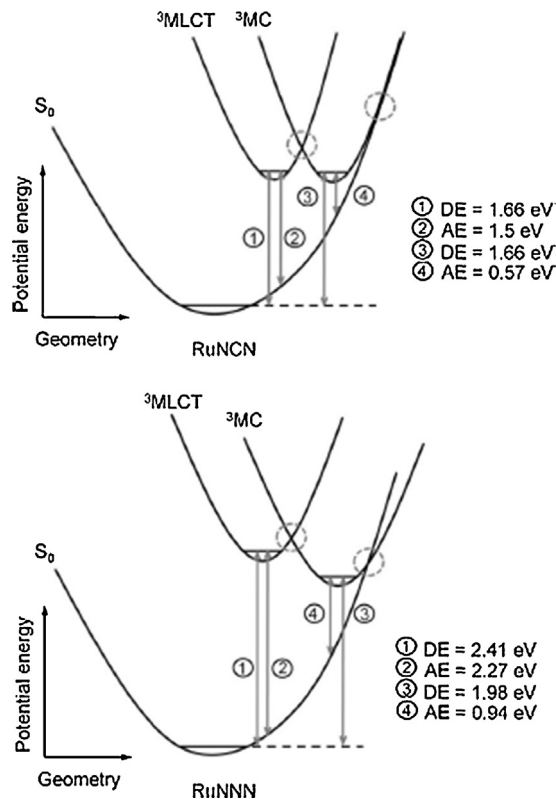
Fig. 8. Proposed potential energy surfaces (the MLCT′ is omitted for clarity) including adiabatic (AE) and diabatic energies (DE) at the DSCF-PCM-DFT/6-31G* level of theory for the complexes RuNCN (top) and RuNNN (bottom).

to rationalize the absorption and emission spectra. A year later Schulze et al. [252] reported the synthesis of a series of heteroleptic bis(tridentate)ruthenium(II) complexes of click-derived 1,3-bis(1,2,3-triazol-4-yl)benzene NĈN coordinating ligands aimed toward the application in dye-sensitized solar cells. The new complexes were analyzed by single crystal X-ray diffraction, and their photophysical and electrochemical properties were studied by computational methods. The potential energy surfaces for the complexes RuNCN and RuNNN are depicted schematically in Fig. 8.

The diabatic energies (DEs) are obtained as the energetic differences between the energy minima of the optimized geometries, while the adiabatic energies (AEs) are obtained as the actual energy differences at the ^{3}MLCT and the ^{3}MC optimized geometries. As shown in Fig. 8, the ^{3}MLCT and ^{3}MC minima are almost isoenergetic for RuNCN, while for RuNNN the ^{3}MC minimum is lower in energy than the ^{3}MLCT one. This is in agreement with a destabilized ^{3}MC state for RuNCN as a result of the cyclometalation. As an additional consequence, the S$_0$ is destabilized as well and both ^{3}MLCT and ^{3}MC states appear at lower energies relative to the S$_0$. Usually, the subsequent ^{3}MC–S$_0$ intersystem crossing rate is the limiting rate occurring at high energies on the potential energy surfaces for RuNCN, while for RuNNN and [Ru(tpy)$_2$]$^{2+}$ this ^{3}MC–S$_0$ intersystem crossing point is at low energies and thus readily accessible. The resulting small S$_0$–^{3}MLCT energy gap leads to a more probable thermally non-activated, radiationless deactivation due to an increased Franck–Condon overlap of the S$_0$ and ^{3}MLCT vibrational wave functions.

The photophysical properties of Ni(II), Pd(II), Pt(II) and Pt(IV) complexes have recently investigated by means of relativistic zeroth-order regular approximation (ZORA/DFT/TD-DFT) calculations on model systems where spin-orbit coupling (SOC) effects

are explicitly considered [253]. The blue shift of the Q-band along the Ni(II), Pd(II) and Pt(II) series of complexes was interpreted on the basis of the metal-induced electronic structure changes. The complexes exhibited also a distinct near-infrared (NIR) absorption due to a transition to the double-group ^1E (π,π^*) state, which is dominated by the lowest single-group ^3E (π,π^*) state. Unlike Ni(II) complex, which is nonluminescent, Pd(II) and Pt(II) complexes show both deep red fluorescence emission and NIR phosphorescence emission. The fluorescence and phosphorescence emissions occur from the $S_1(\pi,\pi^*)$ and $T_1(\pi,\pi^*)$ states, respectively. Owing to their triplet properties, the Pd(II) and Pt(II) complexes can be considered promising photosensitizers for use in photodynamic therapy (PDT) and potential candidates for near-infrared (NIR) light emitting diodes or NIR emitting probes. The photochemistry of Pt(IV) complexes with general formula $[Pt(X)_2(Y)_2(Z)_2]^{o/-}$ (X = N-ligands (NH$_3$, pyridine, etc.)/S(CH$_3$)$_2$/H$^-$, Y = (pseudo)halogen (N$_3^-$, I$^-$), Z = OR$^-$, R = H, Ac) was also investigated by TD-DFT simulation of their optical properties [254]. Calculated excitation energies for the intense band according to TD-DFT with the SAOP functional are in good agreement with experimental observations. An unusual polymer metallic chain system $[\{Pt(bzq)(C_6F_5)_2\}Ag]_n$ and a series of bimetallic $[\{Pt(bzq)(C_6F_5)_2\}AgL]$ complexes stabilized by short Pt–Ag (2.75 Å) and η^1 Ag$\cdots$C(bzq) ($\sim$2.45 Å) bonding interactions have been constructed starting from the anionic $[Pt(bzq)(C_6F_5)_2]^-$ building block [255]. The bonding and photophysical properties (absorption and emission) have been studied by means of DFT and TD-DFT calculations to obtain greater insight into the influence of d^8–d^{10} metallophilic bonds on the nature of the electronic transitions. Assignments of all absorption and emission bands are given. Absorption and emission of the polymer in the solid state is suggested to be associated with an electronic transition of a mixed $[Pt(bzq) \rightarrow Ag]/[Ar_f \rightarrow Ag]$ character.

Recently we employed electronic structure calculation methods (DFT and TD-DFT) to study the $Pt_3(\mu_2\text{-}L)_3(L')_3$ clusters and the $[(\mu_3\text{-}Tl)Pt_3(\mu_2\text{-}L)_3(L')_3]^+$ (L = CO, SnR$_2$, SnH$_2$, SiR$_2$, SiH$_2$, CH$_3$CN, PH$_2$, C$_6$F$_5$, SO$_2$ or HCN and L' = CO, PH$_3$, CH$_3$CN, C$_6$F$_5$, HCN) half-sandwiches [256]. Mulliken, NBO and CDA analyses indicate that electron density is transferred from the $Pt_3(\mu_2\text{-}L)_3(L')_3$ toward Tl(I) which acquires a cationic charge smaller than 1+. EDA calculations further illustrated the dominance of the covalent and electrostatic interactions between $Pt_3(\mu_2\text{-}L)_3(L')_3$ and Tl(I) with an additional small contribution from dispersion forces. The simulated absorption spectra exhibit absorption bands in the UV region and the shape of NTOs reveals that the "hole" is mainly located on the metal atoms and to a lesser extent on the bridging ligands upon electronic transitions comprising the high energy bands appearing between 220 and 250 nm. On the other hand, the emission maxima are found in the IR region of the spectra. Due to the computed large S_0–T_1 energy gaps, these compounds are expected to exhibit high phosphorescence radiative rate constants, k_r. The $Pt_3(\mu_2\text{-}L)_3(L')_3$ clusters are worth to be investigated for potential use in MOFETs as p-type semiconductors, since they are expected to be good π-bases. Finally, the $Pt_3(\mu_2\text{-}L)_3(L')_3$ clusters exhibit deep HOMO and LUMO energies making them attractive to be considered for use in LED devices. We also investigated a series of "full-face" $\{(\mu_6\text{-}Tl)[Pt_3(\mu_2\text{-}L)_3(L')_3]_2\}^+$ (L = CO, CH$_3$CN, PH$_2$, C$_6$F$_5$, or SO$_2$ and L' = CO, PH$_3$, CH$_3$CN, C$_6$F$_5$) inorganic thaliocenes employing DFT and TD-DFT methods combined with NBO, CDA and EDA electronic structure calculation techniques [257]. The "full-face" inorganic thaliocenes constructed from the coordination of $Pt_3(\mu_2\text{-}L)_3(L')_3$ decks to Tl(I) adopt a bent titanocene like configuration. The $Pt_3\cdots Tl^+\cdots Pt_3$ bonding mode was validated by EDA calculations which demonstrated that the electrostatic and covalent components of the interaction contribute almost equally to the bonding interactions. CDA and NBO calculations indicated that charge transfer from Tl$^+$ cation to the Pt$_3$(0) {3:3:3} decks also occurs. The

TD-DFT simulated absorption spectra of the $\{[Pt_3(\mu_2\text{-}L)_3(L')_3]_2(\mu_3\text{-}Tl)\}^+$ inorganic thaliocenes showed bands mainly in the region of 300–500 nm of the absorption spectra and are strongly red shifted with respect to the absorption spectra of the "open-face" $\{[Pt_3(\mu_2\text{-}L)_3(L')_3](\mu_3\text{-}Tl)\}^+$ half-sandwiches. These bands are assigned as MLCT/MC transitions. The absorption bands are mainly of MLCT/MC character while phosphorescence is predicted to occur via the first triplet excited state, T_1 since the spin density of this excited state could be described as a SOMO-1/SOMO combination.

A computational benchmarking of the structural and optical properties of a bis(chelate) copper(I) guanidine–quinoline complex employing the linear response approach to TD-DFT [258]. The geometric benchmarking recommends the BP86/6-311G(d) computational protocol for best accordance of gas-phase calculations to the solid state structures from X-ray measurements whereas the optical benchmarking gives best resemblance to experimental spectra when applying the B3LYP/def2-TZVP computational protocol. From the comparison between TD-DFT and many-body perturbation theory (MBPT), it is concluded that at least the low-energy excitations are remarkably robust with respect to the approximations made in their description. While MBPT methods are for computational reasons not yet applicable to large bis(chelate) copper complexes, the present results indicated that their excitations can be meaningfully modeled within TD-DFT. Hence, provided a careful benchmarking is performed, CT excitations in copper complexes are accessible to a quantitative analysis based on DFT.

The nature of the ground and excited states involved in the reported luminescent behavior of $[Ag_3\{(pyCH_2)_2im\}_3]^{3+}$ (**1**) and $[Ag_3\{(pyCH_2)_2bzim\}_3]^{3+}$ (**2**) (py = pyridine, im = imidazole, and bzim = benzimidazole) complexes, involving the $[Ag_3]^{3+}$ core stabilized by pyridyl derivatives of N-heterocyclic carbenes were assessed by Muñoz-Castro [259] employing relativistic DFT calculations including scalar and spin-orbit coupling. The calculated electronic excitations including spin-orbit coupling allowed one to determine that the metal–ligand to ligand charge transfer transitions are responsible for the luminescent properties of the complexes leading to slightly distorted structures. Complexes **1** (**2**) absorbing at 298 nm (320 nm) and emitting at 441 nm (460 nm) lead to radiative transitions resulting in calculated Stokes shifts of 10881 cm^{-1} (9511 cm^{-1}). However, such Stokes shifts are enormous, likely indicating that the absorption band quoted is not the emitting state. Probably there should be a lower emitting state, possibly not seen in the absorption spectrum, which is the actual emitting state. Accordingly, the calculated Stokes shift is not calculated properly since it should be the energy difference between the actual 'unseen' absorption state and the emission state.

Páez-Hernandez and Arratia-Pérez [260] illustrated the importance of electron delocalization over optical and magnetic properties in inverted-sandwich complexes with the structure $(C_8H_8)M(\mu_2,\eta^8\text{-}C_8H_8)M(C_8H_8)$ (M = Ti, Zr and Th) and their heterobimetallic combinations (Ti–Th and Zr–Th). They also demonstrated the capability of relativistic density functional approach for the calculation of different contributions to Zero-Field-Splitting (ZFS) and the absorption spectrum in homometallic and heterobimetallic molecules. Nucleus independent chemical shift (NICS) calculated at the GIAO-OPBE/TZ2P level illustrated an important electron mobility in the region between two metals in all cases, particularly around the z axis, indicative for the presence of diatropic currents (aromaticity) and therefore delocalized structure. This electron delocalization allows the strong mix between metal and ring orbitals with a consequent effect over the spin–orbit coupling (SOC) term in the ZFS calculation. Excitation energies, and the electronic transitions over 500 nm were simulated by TD-DFT with the objective to analyze the transition metal role as an antenna effect in the absorption band in the near-IR region. The
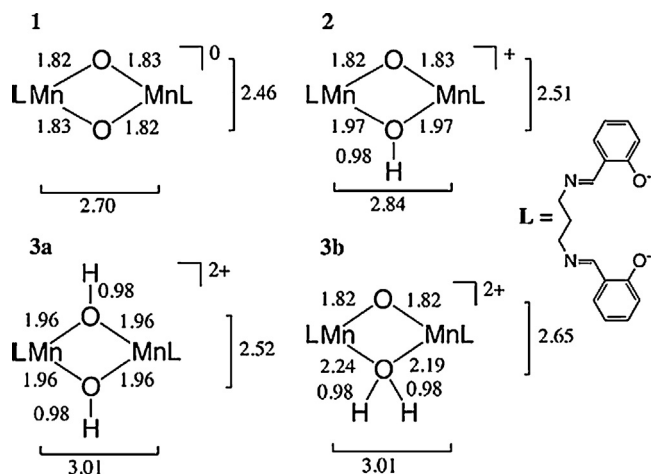
Fig. 9. Representation of the dinuclear $[LMn^{IV}O]_2H_x$ ($x=0$–2) compounds, their total charges and the selected core bond distances from DFT geometry optimization [263]. Reproduced with permission from Ref. [262]. Copyright 2013: The American Chemical Society.

contributions to spin–spin coupling (SS) and SOC to ZFS were analyzed, and the spin density over the metal centers is discussed employing their scheme of metal–metal communication.

Spin-free TD-DFT and MS-CASPT2 calculations reproduce qualitatively the main features of the experimental absorption spectra of $HMn(CO)_5$ and $HRe(CO)_5$ complexes [261]. The spin–orbit (SO) effects on the absorption spectra of these complexes increase the density of electronic excited states leading to a broadening of the theoretical spectra and weakening of the intense bands. The simulated spectra of $HMn(CO)_5$ and $HRe(CO)_5$ show one MLCT band of intermediate intensity around 40,000–42,000 cm^{-1}, which is not observed in the experimental spectra. The main character of the transitions is not affected by the SO corrections and a large mixing between MLCT, MSBCT, SBSBCT, and MC states is observed, especially in the upper part of the absorption spectra of both molecules. The SO absorption spectra are more realistic for both molecules with a red shift of the start of the absorption and a broadening of the bands due to a large mixing between the singlet–triplet states and an increase of the density of electronic states contributing to the absorption. This red shift is more important in $HMn(CO)_5$ than in $HRe(CO)_5$ due to the MC contribution to the lowest states in first-row transition metal complexes.

In two complementary papers, Pecoraro, Yano, Neese, DeBeer and co-workers [262,263] explored the sensitivity of both X-ray absorption (XAS) and X-ray emission spectroscopy (XES) to changes in ligand protonation states of a set of dinuclear bis-μ-oxo-bridged Mn^{IV} [$Mn_2(IV,IV)(\mu$-O$)_2$(salpn$)_2$] complexes (Fig. 9) in different protonation states in combination with DFT calculations.

DFT calculations were performed to simulate the valence-to-core XES spectra and to assign the spectral features to specific transitions. The analysis of the calculated spectra based on either high spin (HS) or broken symmetry (BS) density functional solutions provides nearly identical results: the most intense transitions are into acceptor orbitals from the local e_g set; at lower energies from the 1s-α orbitals, at higher energies from the 1s-β orbitals. The analysis represents the first calculation of metal pre-K-edge spectra for multinuclear complexes using a TD-DFT approach. The effects of spin polarization on the calculated Mn K pre-edge spectra, in both the HS and BS solutions, are discussed in terms of the strength of the antiferromagnetic coupling and associated changes in the covalency of Mn—O bonds. The accompanying paper [262] on X-ray emission spectroscopy (XES) of the same compounds demonstrates that valence-to core XES provides a complementary probe.

In this study, the authors demonstrated that XES valence to core spectra probe the ligand environment of metals with great sensitivity, including single protonation events. In particular, the Kβ″ satellite peaks can be used to discriminate among a set of three Mn^{IV} dimers in which the protonation states of bridging oxygen atoms are changed systematically. Together, XAS and XES methods provide powerful element-specific tools to monitor changes in the ligand environment in metalloproteins, possibly during catalysis, by neglecting the overwhelming number of surrounding light atoms and promise for obtaining insight into the protonation changes which occur in the S states of the Kok cycle and hence ultimately the mechanism of photosynthetic water oxidation.

Electronic excitations and detachments of MnO_4^- and TcO_4^- have been calculated, employing *ab inito* WFT methods CR-EOM-CCSD(T) and RAS-PT2 (CR = completely renormalized; EOM = equation of motion; CC = coupled cluster; SD(T) = single, double, and perturbative triple substitutions; RAS = self-consistent restricted active space; PT2 = second order perturbation theory) and DFT approaches [264]. TD-DFT without proper correction of the self-interaction error (SIE) is not recommendable for the electronic excitations of such complexes, although one obtains reasonably small deviations for TcO_4^-, probably due to fortuitous error cancelation. The authors presented the first study of the excited states of MnO_4^- and TcO_4^- using the CR-EOM-CCSD(T) and RASPT2 methods. The results illustrated that both dynamic and nondynamic electron correlations are very important in the ground and excited states of MnO_4^- and TcO_4^-. Especially, the nondynamic electron correlation of MnO_4^- can already be well recovered at the quadruple substitution level based on the RASSCF calculations. Remarkably, larger active spaces and higher electronic substitutions are needed for reliable excitation energy predictions of the heavier homologue TcO_4^-, which is also bound more strongly.

3.4. Simulation of heavy-nucleus NMR chemical shifts of coordination compounds by DFT

Evaluation of NMR parameters has become an important application of quantum chemistry over the last two decades. In the following we review recent successful applications of DFT methods for prediction of heavy-nucleus NMR chemical shifts of coordination compounds.

Autschbach [265] reported an overview of theoretical work related to magnetic-field perturbations of metal complexes. It was demonstrated by a range of applications of DFT and TD-DFT-based theoretical methods that their overall performance for metal complexes is quite good. Relativistic methods permit computations on molecules that contain elements from all parts of the periodic table. The inclusion of solvent effects can be vital for reproducing experimental results. Particularly NMR parameters of metal complexes appear to be sensitive to solvent effects.

For high accuracy in the calculated NMR shielding constants a carefully selected basis set that properly describes the outer-core–inner-valence region is necessary; at the same time, it must be constructed in a manner that allows for a systematic improvement in the description of the correlation energy [266]. For heavier elements, relativistic effects are important, not only for the shielding of the heavy atoms (HAHA effects) but also for light elements in close proximity to a heavy element (HALA effects). This HALA effect arises because spin-orbit coupling at the heavy atom induces a spin polarization of the electrons that couples (by the Fermi-contact and spin-dipole mechanisms) to the nuclear magnetic moment of the nearby light atom in the same way that this nuclear moment couples to the spin polarization induced by other nuclei [267].

Wrackmeyer et al. [268] investigated three series of ferrocenes, derived from aminoferrocene Fc-NH$_2$ and 1,1′-diaminoferrocene

Fc(NH$_2$)$_2$, by ^{57}Fe NMR spectroscopy. Structures of the ferrocene derivatives have been optimized for the gas phase by DFT calculations, and ^{57}Fe NMR shieldings were calculated using these geometries employing the GIAO-B3LYP/6−311 + G(d,p) computational protocol. Calculated and experimental data are in reasonable agreement.

An analysis scheme for static linear response properties employing two-component (spin-orbit) relativistic DFT along with scalar relativistic NLMOs and NBOs has been extended to gauge-including atomic orbital (GIAO) shielding tensors by Autschbach [269]. Computations on a number of small molecules and metal complexes have shown that the analysis in terms of localized molecular orbitals yields quite intuitive results. The work was focused on the presentation of the formalism and the validation of the implementation.

^{195}Pt NMR chemical shifts were calculated from two-component relativistic density DFT along with scalar relativistic NLMOs and NBOs [270]. Seven chemical shifts in six Pt complexes with Pt oxidation states II, III, and IV; and halide, amino, and amidate ligands were analyzed, with particular focus on the role of nonbonding Pt 5d orbitals. The spin–orbit effects on the chemical shifts of [PtCl$_4$]$^{2-}$ compared to [PtBr$_4$]$^{2-}$ have also been analyzed.

The implementation of a fast and accurate algorithm for the calculation of the NMR shielding tensor with STOs and the ZORA Hamiltonian with spin-orbital coupling was reported by Krykunov, Ziegler, and van Lenthe [271]. This method was tested on 5d transition-metal complexes employing the B3LYP, BLYP and BP86 DFs. The B3LYP results for the ^{195}Pt NMR chemical shifts are slightly improved with respect to experiment for over the BP86 and BLYP values. For the other systems, use of the B3LYP method does not improve the agreement with experiment compared to results from pure BP86 and BLYP DFs.

The ^{89}Y NMR shifts in a variety of organometallic molecules were calculated with DFT/GIAO methods employing a wide range of DFs [272]. Despite systematic error in the absolute values of the shielding constants, a highly linear fit between calculated and observed shifts exists across a nearly 1300 ppm range. These linear fits lead to further testing O3LYP, mPW1PW91, PBE1PBE, and OLYP DFs as the most promising candidates. For most complexes, agreement within 70 ppm between calculated and experimental shifts is found; for some classes of complexes, such as methylcyclopentadienyl species, the maximum discrepancy is usually half this.

The influence of the optimized effective potential (OEP) and Coulomb-attenuation on shielding constants and chemical shifts was investigated by Tozer and co-workers [273] for three disparate categories of molecules: main group, hydrogen bonded, and transition metal systems. This study reiterated the importance of the OEP procedure in magnetic response calculations using orbital dependent functionals, together with the need for careful attention to ensure physically sensible potentials are obtained. It also illustrated the utility of Coulomb-attenuated functionals for computing short-range molecular properties. For the molecules considered, OEP-B3LYP and OEP-CAM-B3LYP results remain inferior to those of Keal-Tozer (KT2) GGA DF, which is unsurprising given that the latter was specifically designed to provide accurate magnetic response.

Reasonably accurate ^{195}Pt NMR chemical shifts for a series of [PtX$_{6-n}$Y$_n$]$^{2-}$ (X = Cl, Br and Y = F, I) complexes, were calculated using both gas-phase and the COSMO DFT models [274]. The discrepancies between the experimental and the DFT calculated ^{195}Pt NMR chemical shifts vary for these complexes as a function of the coordinated halide ions, as well as where there is a significant deviation from the octahedral symmetry of the reference compound such as, for example, the geometric *cis/trans* or *fac/mer* isomers. These discrepancies seem to be related to an increase in electronegativity difference $\Delta \chi$ between the two halide ligands in the Pt(IV)

coordination sphere and are likely to occur because of reductions in the computational error cancelation effects, due to subtle deviations from ideal octahedral geometries of particularly mixed halide complex anions the series as well as to inadequate modeling of explicit solvent–solute interactions.

It is well established that structural-, vibrational-, solvent-, and relativity-induced shielding effects are of primary importance for the computation of NMR shielding constants and shielding tensors of heavy atoms and, by extension, for the prediction of chemical shifts in inorganic and organometallic systems in solution [275,276]. A combination of ab initio molecular dynamics and relativistic NMR methods based on DFT allowed Truflandier and Autschbach [277] to overcome these intricacies, leading for their test set to an agreement within 10% for the calculated ^{195}Pt chemical shifts with respect to the liquid-state NMR experiments. ^{195}Pt NMR shielding constants were computed with DFT as averages over the aiMD trajectories, using the two-component relativistic zeroth-order regular approximation (ZORA) in order to treat relativistic effects on the Pt shielding tensors. The authors concluded that ^{195}Pt liquid-state NMR parameters may give access to information about the solvation shell organization, for instance. It was also demonstrated that the different behavior of ^{195}Pt NMR parameters with respect to the solvent effects can be directly connected to the solution structure of the complex.

Truflandier, Sutter, and Autschbach [278] investigated the influences of solvent effects and dynamic averaging on the ^{195}Pt NMR shielding and chemical shifts of cisplatin and three cisplatin derivatives in aqueous solution were computed using explicit and implicit solvation models. Within the GGA DFT framework, it was demonstrated that the combination of Car-Parrinello ab initio molecular dynamics (aiMD) with the spin-orbit ZORA relativistic NMR calculations allows one to accurately predict ^{195}Pt NMR chemical shifts of cisplatin derivatives in aqueous solution, with less than 5% deviation from experiment. Comparisons with computationally less demanding implicit solvent models show that error cancelation is ubiquitous when dealing with liquid-state NMR simulations. For the complexes studied, the good performance relies on a cancelation of sizable solvent and vibrational effects on the metal shielding. In a following paper [279], the authors further validated the computational protocol for Pt–N spin–spin coupling constants. The key factors contributing to the magnitude of coupling constants were elucidated, with the most significant being the presence of solvent as well as the quality of the density functional and basis set combination.

More recently Sutter and Autschbach [280] studied the ^{195}Pt, ^{14}N, and ^{15}N NMR data for five platinum azido (N$_3^-$) complexes using relativistic DFT methods. Good agreement with experiment is obtained for Pt and N chemical shifts as well as Pt–N J-coupling constants. The p-rich σ bonding and the delocalized π bonding in azide, along with changes in the azide electronic structure upon the formation of dative N–Pt covalent bonds, can be linked directly to the observed NMR trends. The direct correspondence between the chemical bonding in the azido ligand and observed NMR trends has been established with the help of an analysis of the results of first-principles theoretical calculations in terms of localized molecular orbitals (LMOs).

A complete benchmark study of the molecular DFT computations of solid-state ^{95}Mo nuclear magnetic resonance (NMR) properties of molybdenum hexacarbonyl has been reported [281]. Both quadrupolar interaction and chemical shielding parameters have been computed while varying f_{xc} functional, basis sets and relativistic corrections and compared with parameters of high precision determined using single-crystal ^{95}Mo NMR experiments. The isotropic parameter of both chemical shift and chemical shielding, computed NMR parameters are more sensitive to geometrical variations than computational details. Relativistic effects do not play a

crucial part in the calculations of such parameters for the $4d$ transition metal, in particular isotropic chemical shift. Among the DFs tested hybrid DFs perform better than LDA and GGA DFs for the computations of these isotropic parameters: B3LYP combined with the most extended all-electron triple-z basis set leads to δ_{iso} equal to -1883 ppm for the optimized geometry; the experimental value is -1854 ppm.

The performance of three different relativistic methods in the calculation of NMR shielding constants and Hg chemical shifts in linear HgL_2 (L = Cl, Br, I, CH_3) compounds was studied employing the fully relativistic four-component approach and the two-component approximations, linear response elimination of small component (LR-ESC) and zeroth-order regular approximation (ZORA) [282]. LR-ESC reproduces successfully the four-component results for the C shielding constant in $Hg(CH_3)_2$ within 6 ppm, but fails to reproduce the Hg shielding constants and chemical shifts. For the C shielding constant both LR-ESC and ZORA reproduce the relativistic corrections and, therefore, the absolute value of the shielding constant obtained by the four-component approach. For Cl and Br these methods behave differently: LR-ESC underestimates the relativistic corrections, whereas ZORA overestimates the relativistic corrections to the shielding constants. For iodine LR-ESC overestimates relativistic corrections, while ZORA even gives the incorrect sign of the relativistic correction. The differences between Hg chemical shift values obtained using ZORA and four-component approaches without spin-density contribution to the XC kernel are less than 60 ppm for all compounds using three different functionals, BP86, B3LYP, and PBE0. Hybrid functionals (B3LYP and PBE0) containing HF exchange lead to smaller reductions compared to GGA/BP86 and, therefore, results in better agreement with HF results. For the ZORA calculations it is necessary to use large basis sets (QZ4P) and the TZ2P basis set may give errors of ~500 ppm for the Hg chemical shifts, despite deceivingly good agreement with experimental data.

Relativistically corrected Breit–Pauli perturbation theory (BPPT) Hartree–Fock and DFT results for metal nuclear shieldings and chemical shifts were compared for the group-12 compounds $M(CH_3)_2$ and $[M(H_2O)_6]^{2+}$ systems (M = Zn, Cd, Hg) with M^{2+} ions as the chemical shift reference [283]. It was shown that five out of the total of sixteen BPPT correction terms are responsible for most of the relativistic corrections for the chemical shift of studied metals. The most important result is the fact that the HF chemical shifts are very close to the 4-component values until the sixth row of the periodic table. At the non-relativistic (NR) level it is seen that the correlated ab initio shielding constants and chemical shifts are located between the HF and DFT results, with non-negligible differences between the methods.

Pickard and Mauri [284] performed first-principles calculations of NMR parameters using the gauge including projection augmented wave (GIPAW) method that permits the calculation of NMR chemical shifts with a pseudopotential approach. All applications to date of the GIPAW method in chemistry and materials science has recently been reviewed [285]. Multinuclear solid-state nuclear magnetic resonance (SSNMR) experiments have been performed on cisplatin and four related square-planar compounds by Lucier et al. [286]. Platinum magnetic shielding (MS) tensor orientations were calculated using both plane-wave density functional theory (DFT) and standard DFT methods. Plane-wave calculations for these systems consistently predict ^{195}Pt CS tensor parameters to a high degree of accuracy. The observed inconsistency of DFT calculations on isolated molecules indicated that intermolecular interactions may play a significant role in determining the origins of the ^{195}Pt CS tensor parameters and orientations.

Aquino, Pritchard and Autschbach [287] reported a method by which calculated hyperfine coupling constants (HFCCs) and paramagnetic NMR (pNMR) chemical shifts can be analyzed in a chemically intuitive way by decomposition into contributions from localized molecular orbitals (LMOs). A new implementation for HFCCs has been carried out in NWChem utilizing the two-component relativistic ZORA Hamiltonian and DFT with non-hybrid functionals, global hybrids, and range-separated hybrids. Benchmark calculations on a test set of radicals with few atoms, covering light and heavy main group elements and metal atoms, show that reasonable agreement with experiment can be achieved with spin-unrestricted scalar ZORA DFT calculations of HFCCs. The pNMR chemical shifts for two metallocenes that were analyzed in detail, Ni and V, show that the opposing signs of the chemical shifts and the very different magnitudes are caused by different spin-polarization mechanisms.

The successful computation of accurate ^{195}Pt chemical shifts for a series of *cis*-$(amine)_2PtX_2$ (X = Cl, Br, I), *cis*-bis(amine) Pt(II) anticancer agents with carboxylato- or acetylo- leaving ligands as well as octahedral Pt(IV) anticancer agents in solutions employing the PCM solvation model was achieved employing the non-relativistic GIAO-PBE0/SARC-ZORA(Pt) ∪ 6-31 + G(d)(E) computational protocol [288]. Despite of neglecting relativistic and spin orbit effects the agreement of the calculated δ ^{195}Pt chemical shifts with experimental values is surprising probably due to effective error compensation. Moreover, the observed solvent effects on the structural parameters of the complexes probably overcome the relativistic effects, and therefore the successful applicability of the non-relativistic GIAO-PBE0/SARC-ZORA(Pt) ∪ 6-31 + G(d)(E) computational protocol in producing reliable $\delta_{calcd}(^{195}Pt)$ chemical shifts could be understood.

4. Concluding remarks

In this review, we have attempted to overview recent progress in DFT application to coordination chemistry. The plethora of successful applications of DFT in coordination chemistry renders DFT a general tool for understanding and predicting the behavior of a broad range of chemical, physical, and biological phenomena of importance in chemical reactivity, catalytic activity, bioactivity, photophysics, electronic and nuclear-magnetic resonance spectroscopy, linear and nonlinear optics etc. Particular emphasis was given to the practical aspects that may be interesting for experimentalists that wish to employ DFT alongside to their experimental work. We have attempted to provide a guided tour of the use of DFT in solving problems that arise in coordination chemistry and familiarize the newcomer to the field of computational coordination chemistry with the practical issues faced under DFT at work. The capabilities of DFT along with the DFT tools available are analyzed. For the newcomer to the field the key question is probably: "Which DFT computational protocol should I use for my study?" At the present time, there is no systematic way of choosing the proper DFT computational protocol and the most popular ones in the literature have been derived by careful comparison with experiment. It should be emphasized that great care has to be exercised in choosing the DFT computational protocol to calculate properly spin states in transition metal complexes. To this end some general instructions of how to select the proper DFT computational protocol for a particular study of interest are offered to the nonspecialist in the field of computational coordination chemistry. However, it should be stressed that in coordination chemistry the DFT and TD-DFT calculations have to be validated by rigorous ab initio or by accurate experimental data for each new problem or new system, particularly when investigating excited states.

References

[1] S. Niu, M.B. Hall, Chem. Rev. 100 (2000) 353.
[2] G.H. Loew, D.L. Harris, Chem. Rev. 100 (2000) 407.

[3] P.E.M. Siegbahn, M.R.A. Blomberg, Chem. Rev. 100 (2000) 421.
[4] M. Torrent, M. Solà, G. Frenking, Chem. Rev. 100 (2000) 439.
[5] M.-M. Rohmer, M. Bènard, J.-M. Poblet, Chem. Rev. 100 (2000) 495.
[6] A. Dedieu, Chem. Rev. 100 (2000) 543.
[7] A. Maseras, A. Lledós, E. Clot, O. Eisenstein, Chem. Rev. 100 (2000) 601.
[8] J.A. Alonso, Chem. Rev. 100 (2000) 637.
[9] J.F. Harrison, Chem. Rev. 100 (2000) 679.
[10] G. Frenking, N. Fröhlich, Chem. Rev. 100 (2000) 717.
[11] N.S. Hush, J.R. Reimers, Chem. Rev. 100 (2000) 775.
[12] A. Ceulemans, L.F. Chibotaru, G.A. Heylen, K. Pierloot, L.G. Vanquickenborne, Chem. Rev. 1009 (2000) 787.
[13] T.R. Cundari, Chem. Rev. 100 (2000) 807.
[14] P. Comba, R. Remaenyi, Coord. Chem. Rev. 238–239 (2003) 9.
[15] D.E. Ellis, O. Warschkow, Coord. Chem. Rev. 238–239 (2003) 31.
[16] J. Autschbach, T. Ziegler, Coord. Chem. Rev. 238–239 (2003) 83.
[17] C. Daniel, Coord. Chem. Rev. 238–239 (2003) 143.
[18] M.D. Newton, Coord. Chem. Rev. 238–239 (2003) 167.
[19] I. Ciofini, C.A. Daul, Coord. Chem. Rev. 238–239 (2003) 187.
[20] T. Lovell, F. Himo, W.-G. Han, L. Noodleman, Coord. Chem. Rev. 238–239 (2003) 211.
[21] H.T. Erras-Hanauer Clark, R. van Eldik, Coord. Chem. Rev. 238–239 (2003) 233.
[22] I.P. Georgakaki, L.M. Thomson, E.J. Lyon, M.B. Hall, M.Y. Darensbourg, Coord. Chem. Rev. 238–239 (2003) 255.
[23] R.A. Friesner, M.-H. Baik, B.F. Gherman, V. Guallar, M. Wirstam, R.B. Murphy, S.J. Lippard, Coord. Chem. Rev. 238–239 (2003) 267.
[24] A.J. Boone, C.H. Chang, S.N. Greene, T. Herz, N.G.J. Richards, Coord. Chem. Rev. 238–239 (2003) 291.
[25] C. Webster, M.B. Hall, Coord. Chem. Rev. 238–239 (2003) 315.
[26] J. Renhold, A. Barthel, C. Mealli, Coord. Chem. Rev. 238–239 (2003) 333.
[27] J.N. Harvey, R. Poli, K.M. Smith, Coord. Chem. Rev. 238–239 (2003) 347.
[28] V.N. Sapunov, R. Schmid, K. Kirchner, H. Nagashima, Coord. Chem. Rev. 238–239 (2003) 363.
[29] P. Macchi, A. Sironi, Coord. Chem. Rev. 238–239 (2003) 383.
[30] L. Noodleman, T. Lovell, W.-G. Han, J. Li, F. Himo, Chem. Rev. 104 (2004) 459.
[31] E.I. Solomon, R.K. Szilagyi, S. DeBeer George, L. Basumallick, Chem. Rev. 104 (2004) 419.
[32] C.A. Tsipis, Comments Inorg. Chem. 25 (2004) 19.
[33] A. Poater, F. Ragone, A. Correa, L. Cavallo, Dalton Trans. 40 (2011) 11066.
[34] P. Chandrasekaran, S. Chantal, E. Stieber, T.J. Collins, L. Que Jr., F. Neese, S. DeBeer, Dalton Trans. 40 (2011) 11070.
[35] G. Aitken, N. Hazari, A.S.P. Frey, F. Geoffrey, N. Cloke, O. Summerscales, J.C. Green, Dalton Trans. 40 (2011) 11080.
[36] M. Besora, C. Gourlaouen, B. Yates, F. Maseras, Dalton Trans. 40 (2011) 11089.
[37] S. Montserrat, I. Alonso, F. López, J.L. Mascareñas, Ag. Lledós, G. Ujaque, DaltonTrans. 40 (2011) 11095.
[38] Y. Gong, L. Andrews, Dalton Trans. 40 (2011) 11106.
[39] H.-G. Cho, L. Andrews, Dalton Trans. 40 (2011) 11115.
[40] J. Su, L. Shi, X. Sun, W. Guan, Z. Wu, Dalton Trans. 40 (2011) 11131.
[41] L.F. Veiros, M.J. Calhorda, Dalton Trans. 40 (2011) 11138.
[42] M. Sundararajan, R.S. Assary, I.H. Hillier, D.J. Vaughan, Dalton Trans. 40 (2011) 11156.
[43] W.-G. Han, G.M. Sandala, D.A. Giammona, D. Bashford, L. Noodleman, Dalton Trans. 40 (2011) 11164.
[44] U. Ryde, R.A. Mata, S. Grimme, Dalton Trans. 40 (2011) 11176.
[45] N. Fey, B.M. Ridgway, J. Jover, C.L. McMullin, J.N. Harvey, Dalton Trans. 40 (2011) 11184.
[46] H. Cox, C. Norris, G. Wu, J. Guan, S. Hessey, A.J. Stace, Dalton Trans. 40 (2011) 11200.
[47] I. Del Rosal, R. Poteau, L. Maron, Dalton Trans. 40 (2011) 11211.
[48] I. Del Rosal, R. Poteau, L. Maron, Dalton Trans. 40 (2011) 11228.
[49] L. Vilella, P. Vidossich, D. Balcells, A. Lledós, Dalton Trans. 40 (2011) 11241.
[50] K.H. Birjkumar, N.D. Bryan, Ni. Kaltsoyannis, Dalton Trans. 40 (2011) 11248.
[51] R. Terrett, G. Cavigliasso, R. Stranger, B.F. Yates, Dalton Trans. 40 (2011) 11267.
[52] M. Jaccob, P. Comba, M. Maurer, P. Vadivelu, P. Venuvanalingam, Dalton Trans. 40 (2011) 11276.
[53] C. Gourlaouen, Ol. Parisel, H. Gérard, Dalton Trans. 40 (2011) 11282.
[54] A. Kubas, J. Hartung, K. Fink, Dalton Trans. 40 (2011) 11289.
[55] X. Li, G. Chen, S. Schinzel, P.E.M. Siegbahn, Dalton Trans. 40 (2011) 11296.
[56] C. Bäcktorp, P.-O. Norrby, Dalton Trans. 40 (2011) 11308.
[57] C. Shi, T. Guo, K.C. Poon, Z. Lin, G. Jia, Dalton Trans. 40 (2011) 11315.
[58] A.I. Poblador-Bahamonde, R. Poteau, C. Raynaud, O. Eisenstein, Dalton Trans. 40 (2011) 11321.
[59] C.J. Cramer, D.G. Truhlar, Phys. Chem. Chem. Phys. 11 (2009) 10757.
[60] F. Neese, Coord. Chem. Rev. 253 (2009) 526.
[61] C. Platas-Iglesias, A. Roca-Sabio, M. Regueiro-Figueroa, D. Esteban-Gómez, A. de Blas, T. Rodríguez-Blas, Curr. Inorg. Chem. 1 (2011) 91.
[62] E. Maslowsky Jr., Coord. Chem. Rev. 255 (2011) 2746.
[63] K.P. Kepp, Coord. Chem. Rev. 257 (2013) 196.
[64] P. Hohenberg, W. Kohn, Phys. Rev. 136 (1964) B864.
[65] W. Kohn, L.J. Sham, Phys. Rev. 140 (1965) A1133.
[66] P. Politzer, J.M. Seminario, Modern Density Theory: A Tool for Chemistry, Elsevier Science B.V., Amsterdam, The Netherlands, 1995.
[67] W. Koch, M.C. Holthausen, A Chemist's Guide to Density Functional Theory, Wiley-VCH, Weinheim, 2000.
[68] F. Nogueira, A. Castro, M.A.L. Marques, in: C. Fiolhais, F. Nogueira, M. Marques (Eds.), A Tutorial on Density Functional Theory, LNP 620, Springer-Verlag, Berlin/Heidelberg, 2003, p. 218.
[69] P. Geerlings, F. De Proft, W. Langenaeker, Chem. Rev. 103 (2003) 1793.
[70] J.S.M. Anderson, J. Melin, P.W. Ayers, J. Chem. Theor. Comput. 3 (2007) 358.
[71] J.S.M. Anderson, J. Melin, P.W. Ayers, J. Chem. Theor. Comput. 3 (2007) 375.
[72] L. Goerigk, S. Grimme, J. Chem. Theor. Comput. 7 (2011) 291–309.
[73] W. Kohn, A.D. Becke, R.G. Parr, J. Phys. Chem. 100 (1996) 12974.
[74] R.G. Parr, W. Yang, Density Functional Theory of Atoms and Molecules, Oxford University Press, New York, 1989.
[75] S.H. Vosko, L. Wilk, M. Nusair, Can. J. Phys. 58 (1980) 1200.
[76] J.P. Perdew, Phys. Rev. B 33 (1986) 8822.
[77] J.P. Perdew, Y. Wang, Phys. Rev. B 33 (1986) 8800.
[78] A.D. Becke, Phys. Rev. A 38 (1988) 3098.
[79] J.P. Perdew, Y. Wang, Phys. Rev. B 45 (1992) 13244.
[80] P. Jemmer, P.J. Knowles, Phys. Rev. A 51 (1995) 3571.
[81] A.D. Becke, J. Chem. Phys. 104 (1996) 1040.
[82] A.D. Becke, J. Chem. Phys. 98 (1993) 5648.
[83] C. Lee, W. Yang, R.G. Parr, Phys. Rev. B 37 (1988) 785.
[84] L.A. Curtiss, K. Raghavachari, P.C. Redfern, J.A. Pople, J. Chem. Phys. 106 (1997) 1063.
[85] S. Grimme, J. Chem. Phys. 124 (2006) 034108.
[86] H. Iikura, T. Tsuneda, T. Yanai, K. Hirao, J. Chem. Phys. 115 (2001) 3540.
[87] J. Heyd, G.E. Scuseria, M.J. Ernzerhof, Chem. Phys. 118 (2003) 8207.
[88] T. Yanai, D.P. Tew, N.C. Handy, Chem. Phys. Lett. 393 (2004) 51.
[89] J. Toulouse, F. Colonna, A. Savin, Phys. Rev. A 70 (2004) 062505-1.
[90] J. Toulouse, F. Colonna, A. Savin, J. Chem. Phys. 122 (2005) 014110.
[91] R. Baer, D. Neuhauser, Phys. Rev. Lett. 94 (2005) 043002-1.
[92] O.A. Vydrov, J. Heyd, A.V. Krukau, G.E. Scuseria, J. Chem. Phys. 125 (2006) 074106-1.
[93] J.W. Song, S. Tokura, T. Sato, M.A. Watson, K. Hirao, J. Chem. Phys. 127 (2007) 154109.
[94] A.J. Cohen, P. Mori-Sanchez, W.T. Yang, J. Chem. Phys. 126 (2007) 191109-1.
[95] J.D. Chai, M.J. Head-Gordon, Chem. Phys. 128 (2008) 084106-1.
[96] J.P. Perdew, A. Ruzsinszky, J. Tao, V.N. Staroverov, G.E. Scuseria, G.I. Csonka, J. Chem. Phys. 123 (2005) 062201-1.
[97] S.F. Sousa, P.A. Fernandes, M.J. Ramos, J. Phys. Chem. A 111 (2007) 10439.
[98] A.J. Cohen, P. Mori-Sánchez, W. Yang, Chem. Rev. 112 (2012) 289.
[99] J.P. Perdew, K. Burke, M. Ernzerhof, Phys. Rev. Lett. 77 (1996) 3865.
[100] S. Kurth, J.P. Perdew, P. Blaha, Int. J. Quantum Chem. 75 (1999) 889.
[101] X. Xu, W.A. Goddard III, Proc. Natl. Acad. Sci. U.S.A. 2004 (101) (2004) 2673.
[102] N.C. Handy, A.J. Cohen, Mol. Phys. 99 (2001) 403.
[103] C. Adamo, V. Barone, J. Chem. Phys. 108 (1998) 664.
[104] F.A. Hamprecht, A.J. Cohen, D.J. Tozer, N.C. Handy, J. Chem. Phys. 109 (1998) 6264.
[105] J.B. Krieger, J. Chen, G.J. Iafrate, A. Savin, Electron Correl. Mater. Prop. (1999) 463.
[106] Y. Zhao, N. Gonzalez-Garcia, D.G. Truhlar, J. Phys. Chem. A 109 (2005) 2012.
[107] Y. Zhao, D.G. Truhlar, J. Chem. Phys. 125 (2006) 194101-1.
[108] Y. Zhao, D.G. Truhlar, J. Chem. Theory Comput. 1 (2005) 415.
[109] J. Tao, J.P. Perdew, V.N. Staroverov, G.E. Scuseria, Phys. Rev. Lett. 91 (2003) 146401-1.
[110] T. Van Voorhis, G.E. Scuseria, J. Chem. Phys. 109 (1998) 400.
[111] Y. Zhao, B.J. Lynch, D.G. Truhlar, J. Phys. Chem. A 108 (2004) 2715.
[112] A.D. Boese, J.M.L. Martin, J. Chem. Phys. 121 (2004) 3405.
[113] Y. Zhao, N.E. Schultz, D.G. Truhlar, J. Chem. Phys. 123 (2005) 161103-1.
[114] Y. Zhao, N.E. Schultz, D.G. Truhlar, J. Chem. Theory Comput. 2 (2006) 364.
[115] Y. Zhao, D.G. Truhlar, Theor. Chem. Acc. 120 (2008) 215.
[116] Y. Zhao, D.G. Truhlar, J. Chem. Theory Comput. 4 (2008) 1849.
[117] R. Peverati, D.G. Truhlar, Phys. Chem. Chem. Phys. 14 (2012) 16187.
[118] W.M. Hoe, A.J. Cohen, N.C. Handy, Chem. Phys. Lett. 341 (2001) 319.
[119] X. Xu, W.A. Goddard III, Proc. Natl. Acad. Sci. U.S.A. 101 (2004) 2673.
[120] J.-D. Chai, M. Head-Gordon, J. Chem. Phys. 131 (2009) 174105-1.
[121] S. Grimme, J. Antony, S. Ehrlich, H. Krieg, J. Chem. Phys. 132 (2010) 154104.
[122] L. Göricke, S. Grimme, Phys. Chem. Chem. Phys. 13 (2011) 6670.
[123] S. Kozuch, D. Gruzman, J.M.L. Martin, J. Phys. Chem. C 114 (2010) 20801.
[124] O.A. Vydrov, G.E. Scuseria, J. Chem. Phys. 125 (2006) 234109-1.
[125] S. Steinmann, C. Corminboeuf, W. Wu, Y. Mo, J. Phys. Chem. 115 (2011) 5467.
[126] S. Steinmann, C. Corminboeuf, J. Chem. Theor. Comput. 7 (2011) 3567.
[127] M. Reiher, O. Salomon, B.A. Hess, Theor. Chem. Acc. 107 (2001) 48.
[128] A. Fouqueau, S. Mer, M.E. Casida, L.M. Lawson Daku, A. Hauser, T. Mineva, F. Neese, J. Chem. Phys. 120 (2004) 9473.
[129] A. Fouqueau, M.E. Casida, L.M. Lawson, A. Hauser, F. Neese, J. Chem. Phys. 122 (2005) 044110-1.
[130] N.E. Schultz, Y. Zhao, D.G. Truhlar, J. Phys. Chem. A 109 (2005) 4388.
[131] S.I. Gorelsky, J. Chem. Theor. Comput. 8 (2012) 908.
[132] G.C. Cramer, D.G. Truhlar, Chem. Rev. 99 (1999) 2166.
[133] J.P. Guthrie, J. Phys. Chem. B 113 (2009) 4501.
[134] J. Tomasi, B. Mennucci, R. Cammi, Chem. Rev. 105 (2005) 2999.
[135] A. Klamt, J. Phys. Chem. 99 (1995) 2224.
[136] A.V. Marenich, C.J. Cramer, D.G. Truhlar, J. Phys. Chem. B 113 (2009) 6378.
[137] A.V. Marenich, C.J. Cramer, D.G. Truhlar, C.A. Guido, B. Mennucci, G. Scalmanid, M.J. Frisch, Chem. Sci. 2 (2011) 2143.
[138] C. van Wüllen, in: M. Barysz, Y. Ishikawa (Eds.), Relativistic Methods for Chemists, Challenges and Advances in Computational Chemistry and Physics, vol. 10, Springer, Dordrecht, 2010, p. 191.

[139] J. Autschbach, J. Chem. Phys. 136 (2012) 150902-1.
[140] T. Nakajima, K. Hirao, Chem. Rev. 112 (2012) 385.
[141] C. Chang, M. Pelissier, M. Durand, Phys. Scr. 34 (1986) 394.
[142] E. van Lenthe, E.J. Baerends, J.G. Snijders, J. Chem. Phys. 99 (1993) 4597.
[143] C. Adamo, D. Jacquemin, Chem. Soc. Rev. 42 (2013) 845.
[144] A.D. Laurent, D. Jacquemin, Int. J. Quantum Chem. 113 (2013) 2019.
[145] N. Fey, B.M. Ridgway, J. Jover, C.L. McMullin, J.N. Harvey, Dalton Trans. 40 (2001) 11184.
[146] T. Ziegler, J. Autschbach, Chem. Rev. 105 (2005) 2695.
[147] T.R. Cundari, Computational Organometallic Chemistry, New York, Marcel Decker, 2001.
[148] F. Maseras, A. Lledós, Computational Modeling of Homogeneous Catalysis, Kluwer Academic Publishers, Dordrecht, The Netherlands, 2002.
[149] A. Uhe, S. Kozuch, S. Shaik, J. Comput. Chem. 32 (2011) 978.
[150] S. Kozuch, S. Shaik, Acc. Chem. Res. 44 (2011) 101.
[151] J. Kleimark, A. Hedström, P.-F. Larsson, C. Johansson, P.-O. Norrby, ChemCatChem 1 (2009) 152.
[152] A. Hedström, E. Lindstedt, P.-O.J. Norrby, Organomet. Chem. 748 (2013) 51.
[153] J.I. du Toit, C.G.C.E. van Sittert, H.C.M. Vosloo, J. Organomet. Chem. 738 (2013) 76.
[154] R.H. Grubbs, T.M. Trnka, M.S. Sanforf, in: H. Kurosawa, A. Yamamoto (Eds.), Current Methods in Inorganic Chemistry: Fundamentals of Molecular Catalysis, vol. 3, Elsevier, Amsterdam, 2003.
[155] P. Liu, X. Xu, X. Dong, B.K. Keitz, M.B. Herbert, R.H. Grubbs, K.N. Houk, J. Am. Chem. Soc. 134 (2012) 1464.
[156] Y. Minenkov, G. Occhipinti, V.R. Jensen, Organometallics 32 (2013) 2099.
[157] L. Vigara, M.Z. Ertem, N. Planas, F. Bozoglian, N. Leidel, H. Dau, M. Haumann, L. Gagliardi, C.J. Cramer, A. Llobet, Chem. Sci. 3 (2012) 2576.
[158] J.A. Varela, C. Saá, J. Organomet. Chem. 694 (2009) 143.
[159] A.M. Rodriguez, C. Cebrián, P. Prieto, J.I. García, A. de la Hoz, Á.D. Ortiz, Chem. Eur. J. 18 (2012) 6217.
[160] Z. Yang, H. Yu, Y. Fu, Chem. Eur. J. 19 (2013) 12093.
[161] K.D. Wiese, D. Obst, Top. Organomet. Chem. 18 (2006) 1.
[162] D. Evans, J.A. Osborn, G. Wilkinson, J. Chem. Soc. A (1968) 3133.
[163] U. Gellrich, D. Himmel, M. Meuwly, B. Breit, Chem. Eur. J. 19 (2013) 16272.
[164] M.V. Jiménez, M.I. Bartolomé, J.J. Pérez-Torrente, D. Gómez, F.J. Modrego, L.A. Oro, ChemCatChem 5 (2013) 263.
[165] K.H. Hopmann, A. Bayer, Coord. Chem. Rev. 268 (2014) 59.
[166] K.H. Hopmann, A. Bayer, Organometallics 30 (2011) 2483.
[167] R. Tanaka, M. Yamashita, L.W. Chung, K. Morokuma, K. Nozaki, Organometallics 30 (2011) 6742.
[168] M. García-Melchor, S.I. Gorelsky, T.K. Woo, Chem. Eur. J. 17 (2011) 13847.
[169] S. Tobisch, Chem. Eur. J. 18 (2012) 7248.
[170] A. de Meijere, F. Diedrich (Eds.), Metal-Catalyzed Cross-Coupling Reactions, 2nd ed., Wiley-VCH, Weinheim, Germany, 2004.
[171] M.G. Melchor, A.A.C. Braga, A. Lledós, G. Ujaque, F. Maseras, Acc. Chem. Res. 46 (2013) 2626.
[172] Z. Li, S.-L. Zhang, Y. Fu, Q.-X. Guo, L. Liu, J. Am. Chem. Soc. 131 (2009) 8815.
[173] K.W. Quasdorf, A. Antoft-Finch, P. Liu, A.L. Silberstein, A. Komaromi, T. Blackburn, S.D. Ramgren, K.N. Houk, V. Snieckus, N.K. Garg, J. Am. Chem. Soc. 133 (2011) 6352.
[174] M. Steinmetz, S. Grimme, ChemistryOpen 2 (2013) 115.
[175] A. Marrone, N. Re, R. Romeo, Organometallics 27 (2008) 2215.
[176] P.A. Dub, R. Poli, J. Am. Chem. Soc. 132 (2010) 13799.
[177] O.N. Faza, A.R. de Lera, Top. Curr. Chem. 302 (2011) 81.
[178] B.A. McKeown, H.E. Gonzalez, M.R. Friedfeld, T.B. Gunnoe, T.R. Cundari, M. Sabat, J. Am. Chem. Soc. 133 (2011) 19131.
[179] J. Hassan, M. Sevignon, C. Gozzi, E. Schulz, M. Lemaire, Chem. Rev. 102 (2002) 1359.
[180] R. Berg, B.F. Straub, Beilstein J. Org. Chem. 9 (2013) 2715.
[181] G. Jiménez-Osés, E. Vispe, M. Roldán, S. Rodríguez-Rodríguez, P. Lo'pez-Ram-de-Viu, L. Salvatella, J.A. Mayoral, J.M. Fraile, J. Org. Chem. 78 (2013) 5851.
[182] L. Dang, Z. Lin, T.B. Marder, Organometallics 29 (2010) 917.
[183] Y. Zhao, Y. Liu, S. Bi, Y. Liu, J. Organomet. Chem. 745–746 (2013) 166.
[184] T. Fan, F.K. Sheong, Z. Lin, Organometallics 32 (2013) 5224.
[185] T.J.L. Mustard, D.J. Mack, J.T. Njardarson, P.H.-Y. Cheong, J. Am. Chem. Soc. 135 (2013) 1471.
[186] M. Rudolph, A.K. Hashmi, Chem. Soc. Rev. 41 (2012) 2448.
[187] M.H. Vilhelmsen, A.K. Hashmi, Chem. Eur. J. 20 (2014) 1901.
[188] R.S. Paton, F. Maseras, Org. Lett. 11 (2009) 2237.
[189] O.N. Faza, R.Á. Rodríguez, C.S. López, Theor. Chem. Acc. 128 (2011) 647.
[190] G. Mazzone, N. Russo, E. Sicilia, Organometallics 31 (2012) 3074.
[191] R.S. Mulliken, J. Chem. Phys. 23 (1955) 1833.
[192] A.E. Reed, L.A. Curtiss, F. Weinhold, Chem. Rev. 88 (1988) 899.
[193] S. Dapprich, G. Frenking, J. Phys. Chem. 99 (1995) 9352.
[194] G. Frenking, M. Sola, S.F. Vyboishchikov, J. Organomet. Chem. 690 (2005) 6178.
[195] K. Morokuma, J. Chem. Phys. 55 (1971) 1236.
[196] K. Kitaura, K. Morokuma, Int. J. Quantum Chem. 10 (1976) 325.
[197] T. Ziegler, A. Rauk, Theoret. Chim. Acta 46 (1977) 1.
[198] M. von Hopffgarten, G. Frenking, Comput. Mol. Sci. 2 (2012) 43.
[199] R.F.W. Bader, Atoms in Molecules: A Quantum Theory, Oxford University Press, Oxford UK, 1990.
[200] F. Corté-Guzmán, R.F.W. Bader, Coord. Chem. Rev. 249 (2005) 633.
[201] A.D. Becke, K.E. Edgecombe, J. Chem. Phys. 92 (1990) 5397.
[202] B. Silvi, A. Savin, Nature 371 (1994) 683.

[203] A. Savin, B. Silvi, F. Colonna, Can. J. Chem. 74 (1996) 1088.
[204] E.R. Johnson, S. Keinan, P. Mori-Sánchez, J. Contreras-García, A.J. Cohen, W. Yang, J. Am. Chem. Soc. 132 (2010) 6498.
[205] S. Shil, D. Bhattacharya, S. Sarkar, A. Misra, J. Phys. Chem. A 117 (2013) 4945.
[206] P. Hirva, M. Haukka, M. Jakonen, M.A. Moreno, J. Mol. Model. 14 (2008) 171.
[207] M. Bühl, C. Reimann, D.A. Pantazis, T. Bredow, F. Neese, J. Chem. Theory Comput. 4 (2008) 1449.
[208] A.C. Tsipis, Organometallics 25 (2006) 2774.
[209] Y. Minenkov, G. Occhipinti, V.R. Jensen, J. Phys. Chem. A 113 (2009) 11833.
[210] J. Moens, F. De Proft, P. Geerlings, Phys. Chem. Chem. Phys. 12 (2010) 13174.
[211] A.C. Tsipis, Organometallics 29 (2010) 354.
[212] N. Takagi, A. Krapp, G. Frenking, Inorg. Chem. 50 (2011) 819.
[213] T. Kegl, R. Ponec, L. Kollar, J. Phys. Chem. A 115 (2011) 12463.
[214] R. Kang, H. Chen, S. Shaik, J.N. Yao, J. Chem. Theory Comput. 7 (2011) 4002.
[215] A. Comas-Vives, J.N. Harvey, Eur. J. Inorg. Chem. (2011) 5025.
[216] K.K. Pandey, H. Braunschweig, A. Lledós, Inorg. Chem. 50 (2011) 1402.
[217] L.M.L. Daku, F. Aquilante, T.W. Robinson, A. Hauser, J. Chem. Theory Comput. 8 (2012) 4216.
[218] D.N. Bowman, E. Jakubikova, Inorg. Chem. 51 (2012) 6011.
[219] W. Jiang, N.J. DeYonker, J.J. Determan, A.K. Wilson, J. Phys. Chem. A 116 (2012) 870.
[220] A.C. Tsipis, Phys. Chem. Chem. Phys. 14 (2012) 14917.
[221] A.C. Tsipis, Organometallics 31 (2012) 7206.
[222] L.M. da Costa, S.R. Stoyanov, R.N. Damasceno, J.W.M. de Carneiro, Int. J. Quantum Chem. 113 (2013) 2528.
[223] L.F. Pašteka, T. Rajsky, M. Urbana, J. Phys. Chem. 117 (2013) 4472.
[224] J. Chen, G. Jia, Coord. Chem. Rev. 257 (2013) 2491.
[225] J. Forniés, C. Fortuño, S. Ibáñez, A. Martín, P. Mastrorilli, V. Gallo, A. Tsipis, Inorg. Chem. 52 (2013) 1942.
[226] A.V. Vologzhanina, A.A. Korlyukov, V.V. Avdeeva, I.N. Polyakova, E.A. Malinina, N.T. Kuznetsov, J. Phys. Chem. A 117 (2013) 13138.
[227] A.C. Tsipis, A.V. Stalikas, Inorg. Chem. 51 (2012) 2541.
[228] A.C. Tsipis, A.V. Stalikas, Inorg. Chem. 52 (2013) 1047.
[229] E. Runge, E.K.U. Gross, Phys. Rev. Lett. 52 (1984) 997.
[230] M.E. Casida, in: D.P. Chong (Ed.), Recent Advances in Density Functional Methods, Part I, World Scientific, Singapore, 1995, p. 155.
[231] M.E. Casida, in: J.M. Seminario (Ed.), Recent Developments and Applications in Density Functional Theory, Elsevier, Amsterdam, 1996, p. 155.
[232] M.E. Casida, M. Huix-Rotllant, Annu. Rev. Phys. Chem. 63 (2012) 287 (and references therein).
[233] D. Jacquemin, E.A. Perpete, I. Ciofini, C. Adamo, R. Valero, Y. Zhao, D.G. Truhlar, J. Chem. Theory Comput. 6 (2010) 2071.
[234] L. Goerigk, S. Grimme, J. Chem. Phys. 132 (2010) 184103-1.
[235] J.-W. Song, M.A. Watson, K. Hirao, J. Chem. Phys. 131 (2009) 144108.
[236] M. Schreiber, M. Silva-Junior, S. Sauer, W. Thiel, J. Chem. Phys. 128 (2008) 134110-1.
[237] T. Stein, L. Kronik, R. Baer, J. Am. Chem. Soc. 131 (2009) 2818.
[238] M. Krykunov, M. Seth, T. Ziegler, J. Chem. Phys. 140 (18) (2014) A502.
[239] M. Krykunov, M. Seth, T. Ziegler, J. Chem. Phys. 391 (2011) 11.
[240] D. Jacquemin, B. Mennucci, C. Adamo, Phys. Chem. Chem. Phys. 13 (2011) 16987.
[241] A. Vlček Jr., S. Záliš, Coord. Chem. Rev. 251 (2007) 258.
[242] C. Garino, L. Salassa, Phil. Trans. R. Soc. A371 (2013) 20120134 (and references therein).
[243] R. Terki, L.-P. Simoneau, A. Rochefort, J. Phys. Chem. A 113 (2009) 534.
[244] B. Minaev, H. Egren, F. De Angelis, Chem. Phys. 358 (2009) 245.
[245] N. Tian, D. Lenkeit, S. Pelz, L.H. Fischer, D. Escudero, R. Schiewek, D. Klink, O.J. Schmitz, I. González, M. Schäferling, E. Holder, Eur. J. Inorg. Chem. 2010 (2010) 4875.
[246] Y. Su, L.-H. Kang, Int. J. Quantum Chem. 112 (2012) 2422.
[247] X.-H. Shang, Y.-Q. Liu, J.-J. Su, G. Gahungu, X.-C. Qu, Z.-J. Wu, Int. J. Quantum Chem. 114 (2014) 183.
[248] D. Ramlot, M. Rebarz, L. Volker, M. Ovaere, D. Beljonne, W. Dehaen, L. Van Meervelt, C. Moucheron, A. Kirsch-De Mesmaeker, Eur. J. Inorg. Chem. 2013 (2013) 2031.
[249] X. Qu, Y. Liu, G. Godefroid, Y. Si, X. Shang, X. Wu, Z. Wu, Eur. J. Inorg. Chem. 2013 (2013) 3370.
[250] A. Damas, L.-M. Chamoreau, A.L. Cooksy, A. Jutand, H. Amouri, Inorg. Chem. 52 (2013) 1409.
[251] B. Schulze, D. Escudero, C. Friebe, R. Siebert, H. Görls, U. Köhn, E. Altuntas, A. Baumgaertel, M.D. Hager, A. Winter, B. Dietzek, J. Popp, L. González, U.S. Schubert, Chem. Eur. J. 17 (2011) 5494.
[252] B. Schulze, D. Escudero, C. Friebe, R. Siebert, H. Görls, S. Sinn, M. Thomas, S. Mai, J. Popp, B. Dietzek, L.L. González, U.S. Schubert, Chem. Eur. J. 18 (2012) 4010.
[253] A.V. Soldatova, J. Kim, C. Rizzoli, M.E. Kenney, M.A.J. Rodgers, A. Rosa, G. Ricciard, Inorg. Chem. 50 (2011) 1135.
[254] H.-C. Tai, Y. Zhao, N.J. Farrer, A.E. Anastasi, G. Clarkson, P.J. Sadler, R.J. Deeth, Chem. Eur. J. 18 (2012) 10630.
[255] J. Forniés, S. Ibáñez, E. Lalinde, A. Martín, M.T. Moreno, A.C. Tsipis, Dalton Trans. 41 (2012) 3439.
[256] A.C. Tsipis, G.N. Gkekas, Dalton Trans. 42 (2013) 2201.
[257] A.C. Tsipis, G.N. Gkekas, Dalton Trans. 42 (2013) 8307.
[258] A. Jesser, M. Rohrmüller, W.G. Schmidt, S. Herres-Pawlis, J. Comput. Chem. 35 (2014) 1.
[259] A. Muñoz-Castro, J. Phys. Chem. A 116 (2012) 520.

[260] D. Páez-Hernández, R. Arratia-Pérez, J. Phys. Chem. A 116 (2012) 7584.
[261] H. Brahim, C. Daniel, A. Rahmouni, Int. J. Quantum Chem. 112 (2012) 2085.
[262] V. Krewald, B. Lassalle-Kaiser, T.T. Boron III, C.J. Pollock, J. Kern, M.A. Beckwith, V.K. Yachandra, V.L. Pecoraro, J. Yano, F. Neese, S. DeBeer, Inorg. Chem. 52 (2013) 12904.
[263] B. Lassalle-Kaiser, T.T. Boron III, V. Krewald, J. Kern, M.A. Beckwith, M.U. Delgado-Jaime, H. Schroeder, R. Alonso-Mori, D. Nordlund, T.-C. Weng, D. Sokaras, F. Neese, U. Bergmann, V.K. Yachandra, S. DeBeer, V.L. Pecoraro, J. Yano, Inorg. Chem. 52 (2013) 12915.
[264] J. Su, W.-H. Xu, C.-F. Xu, W.H.E. Schwarz, J. Li, Inorg. Chem. 52 (2013) 9867.
[265] J. Autschbach, Coord. Chem. Rev. 251 (2007) 1796.
[266] P. Manninen, J. Vaara, J. Comput. Chem. 27 (2006) 434.
[267] P. Lantto, J. Chem. Phys. 125 (2006) 184113-1.
[268] B. Wrackmeyer, E.V. Klimkina, H.E. Maisel, O.L. Tok, M. Herberhold, Magn. Reson. Chem. 46 (2008) S30.
[269] J. Autschbach, J. Chem. Phys. 128 (2008) 164112-1.
[270] J. Autschbach, S. Zheng, Magn. Reson. Chem. 46 (2008) S45.
[271] M. Krykunov, T. Ziegler, E. van Lenthe, J. Phys. Chem. A 113 (2009) 11495.
[272] R.E. White, T.P. Hanusa, Organometallics 25 (2006) 5621.
[273] M.J.G. Peach, J.A. Kattirtzi, A.M. Teale, D.J. Tozer, J. Phys. Chem. A 114 (2010) 7179.
[274] M.R. Burger, J. Kramer, H. Chermette, K.R. Koch, Magn. Reson. Chem. 48 (2010) S38.
[275] M. Bühl, Annu. Rep. NMR Spectrosc. 64 (2008) 77.
[276] J. Autschbach, S. Zheng, Annu. Rep. NMR Spectrosc. 67 (2009) 1.
[277] L.A. Truflandier, J. Autschbach, J. Am. Chem. Soc. 132 (2010) 3472.
[278] L.A. Truflandier, K. Sutter, J. Autschbach, Inorg. Chem. 50 (2011) 1723.
[279] K. Sutter, L.A. Truflandier, J. Autschbach, ChemPhysChem 12 (2011) 1448.
[280] K. Sutter, J. Autschbach, J. Am. Chem. Soc. 134 (2012) 13374.
[281] J. Cuny, K. Sykina, B. Fontaine, L. Le Pollès, C.J. Pickard, R. Gautier, Phys. Chem. Chem. Phys. 13 (2011) 19471.
[282] V. Arcisauskaite, J.I. Melo, L. Hemmingsen, S.P.A. Sauer, J. Chem. Phys. 135 (2011) 044306-1.
[283] J. Roukala, A.F. Maldonado, J. Vaara, G.A. Aucar, P. Lantto, Phys. Chem. Chem. Phys. 13 (2011) 21016.
[284] C.J. Pickard, F. Mauri, Phys. Rev. B 63 (2001) 245101.
[285] C. Bonhomme, C. Gervais, F. Babonneau, C. Coelho, F. Pourpoint, T. Azaïs, S.E. Ashbrook, J.M. Griffin, J.R. Yates, F. Mauri, C.J. Pickard, Chem. Rev. 112 (2012) 5733.
[286] B.E.G. Lucier, A.R. Reidel, R.B. Schurko, Can. J. Chem. 89 (2011) 919.
[287] F. Aquinoa, B. Pritchard, J. Autschbach, J. Chem. Theory Comput. 8 (2012) 598.
[288] A.C. Tsipis, I.N. Karapetsas, Dalton Trans. 43 (2014) 6409.